Inorganic Chemistry

pubs.acs.org/IC Article

# Intracellular Localization Studies of the Luminescent Analogue of an Anticancer Ruthenium Iminophosphorane with High Efficacy in a Triple-Negative Breast Cancer Mouse Model

Kirill Miachin, Virginia Del Solar, Elsy El Khoury, Nazia Nayeem, Anton Khrystenko, Patricia Appelt, Michelle C. Neary, Daniela Buccella,* and Maria Contel*

Cite This: *Inorg. Chem.* 2021, 60, 19152−19164 Read Online

ACCESS | Metrics & More | Article Recommendations | Supporting Information

**ABSTRACT:** The potential of ruthenium(II) compounds as an alternative to platinum-based clinical anticancer agents has been unveiled after extensive research for over 2 decades. As opposed to cisplatin, ruthenium(II) compounds have distinct mechanisms of action that do not rely solely on interactions with DNA. In a previous report from our group, we described the synthesis, characterization, and biological evaluation of a cationic, water-soluble, organometallic ruthenium(II) iminophosphorane (IM) complex of *p*-cymene, ([($\eta^6$-*p*-cymene)Ru{($Ph_3P$═N-CO-2N-$C_5H_4$)-κ-N,O}Cl]Cl (**1** or Ru-IM), that was found to be highly cytotoxic against a panel of cell lines resistant to cisplatin, including triple-negative breast cancer (TNBC) MDA-MB-231, through canonical or caspase-dependent apoptosis. Studies on a MDA-MB-231 xenograft mice model (after 28 days of treatment) afforded an excellent tumor reduction of 56%, with almost negligible systemic toxicity, and a favored ruthenium tumor accumulation compared to other organs. **1** is known to only interact weakly with DNA, but its intracellular distribution and ultimate targets remain unknown. To gain insight on potential mechanisms for this highly efficacious ruthenium compound, we have developed two luminescent analogues containing the BOPIPY fluorophore (or a modification) in the IM scaffold with the general structure of [($\eta^6$-*p*-cymene)Ru{(BODIPY-$Ph_2P$═N-CO-2-$NC_5H_4$)-κ-N,O}Cl]Cl {BODIPY-$Ph_2P$ = 8-[(4-diphenylphosphino)phenyl]-4,4-dimethyl-1,3,5,7-tetramethyl-2,6-diethyl-4-bora-3a,4a-diaza-*s*-indacene (**3a**) and 4,4-difluoro-8-[4-[[2-[4-(diphenylphosphino)benzamido]ethyl]carbamoyl]phenyl]-1,3,5,7-tetramethyl,2,6-diethyl-4-bora-3a,4a-diaza-*s*-indacene (**3b**)}. We report on the synthesis, characterization, lipophilicity, stability, luminescence properties, and cell viability studies in the TNBC cell line MDA-MB-231, nonmalignant breast cells (MCF10a), and lung fibroblasts (IMR-90) of the new compounds. The ruthenium derivative **3b** was studied by fluorescence confocal microscopy. These studies point to a preferential accumulation of the compound in the endoplasmic reticulum, mitochondria, and lysosomes. Inductively coupled plasma optical emission spectrometry (ICP-OES) analysis also confirms a greater ruthenium accumulation in the cytoplasmic fraction, including endoplasmic reticulum and lysosomes, and a smaller percentage of accumulation in mitochondria and the nucleus. ICP-OES analysis of the parent compound **1** indicates that it accumulates preferentially in the mitochondria and cytoplasm. Subsequent experiments in **1**-treated MDA-MB-231 cells demonstrate significant reactive oxygen species generation.

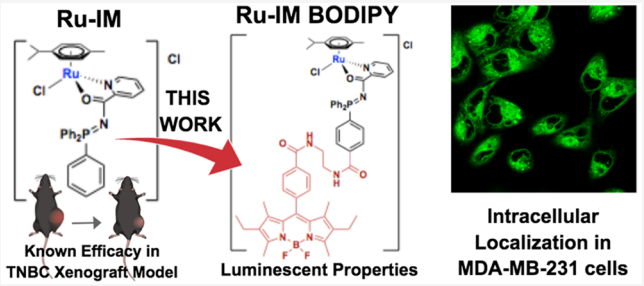




## INTRODUCTION

Breast cancer incidence is increasing around the world, although incidence rates vary widely.[1] For women from regions characterized by lower indices of development and/or income breast cancer mortality is the highest for all cancers, and the second most frequent from regions characterized by higher indices of development and/or income, after lung cancer.[1] Of the different types of breast cancer, triple-negative breast cancer (TNBC) has the worse prognosis and chance of survival, as well as a higher relapse within 5 years after diagnosis compared to estrogen receptor (ER)-positive tumors. TNBC disproportionately affects women of African and Hispanic descent.[2−6] TNBC is a subtype for which estrogen and progesterone receptors and human epidermal growth factor receptor 2 (ER/PR/HER-2) are not expressed. TNBCs are transcriptionally heterogeneous, with the "molecular heterogeneity" described as one of the key morbidity factors.[7] The current treatments for TNBC are based on chemotherapeutic agents administered prior to surgical or radiation interventions because conventional HER-2 targeting and

Received: September 22, 2021
Published: November 30, 2021

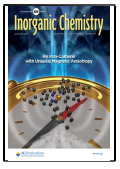





https://doi.org/10.1021/acs.inorgchem.1c02929
*Inorg. Chem.* 2021, 60, 19152−19164

**Chart 1. Anticancer Ruthenium(II) Compound Previously Described ([($\eta^6$-p-Cymene)Ru{($Ph_3P$=N-CO-2$NC_5H_4$)-$\kappa$-N,O}Cl]Cl (Ru-IM, 1) and the New Luminescent Analogues Reported Here[a]**

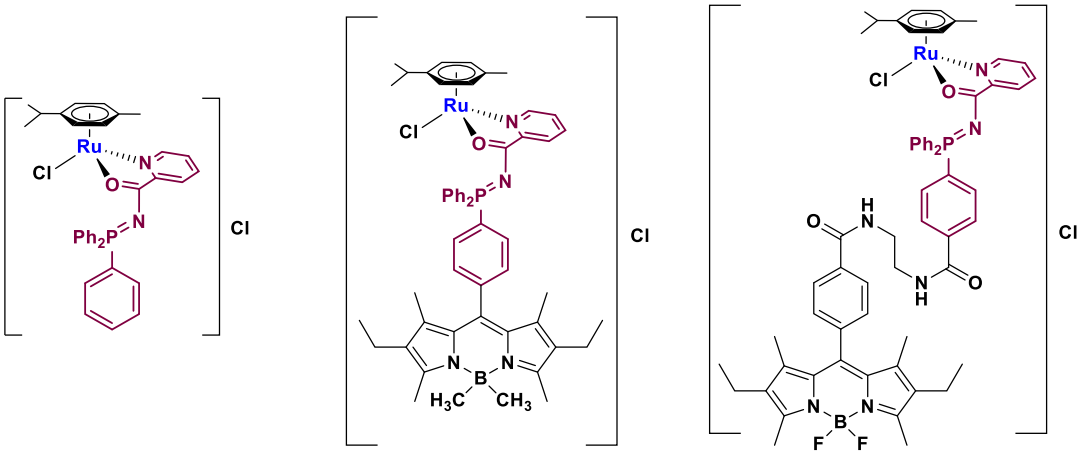


[a]The reaction conditions to obtain **3a** and **3b** are depicted in Scheme 1 and explained in detail in the Experimental Section.

hormone therapies have not been very successful.[8] The most commonly used chemotherapeutics target cell proliferation (anthracycline), DNA repair (platinum compounds), and p53 pathways (taxanes).[9] Recent clinical trials have explored the use of chemotherapeutics in combination therapy[10] (administered with checkpoint, kinase, growth factor receptor inhibitors or monoclonal antibodies) or immunotherapy[9] treatments. In most cases, it seems that the use of a chemotherapeutic agent (alone, in combination therapy, or as an antibody−drug conjugate[11]) affords the best results for aggressive or metastatic TNBCs in terms of a more favorable prognosis.

The use of small molecules as TNBC chemotherapeutics has recently been reviewed, with examples of organometallic compounds.[12] In 2021, we have published a review on metallodrugs as potential chemotherapy agents for TNBCs including recent clinical trials involving conventional platinum compounds.[13] The use of platinum agents for the treatment of TNBC (as adjuvants) is receiving increased attention. Platinum compounds are being considered for TNBC subtypes that do not respond well to standard chemotherapy like anthracycline−taxane neoadjuvant combinations[7,8] or for patients who have BRCA mutations.[8] We also provided a thorough review of different metal-based compounds with a focus on those that have been efficacious *in vivo* and for which preliminary mechanistic studies are available [with examples of nonconventional platinum(II), platinum(IV), gold(III), and ruthenium(II) derivatives].[13]

Ruthenium(II) compounds are gaining attention as alternatives to platinum-based clinical anticancer agents. They have shown specific activity against metastasized solid tumors and tumors that have developed resistance to cisplatin and display modes of action that differ from that of cisplatin.[14] Ruthenium(II) compounds have distinct mechanisms of action that do not rely solely on interactions with DNA.[15] Moreover, there are ongoing clinical trials with two ruthenium compounds. Ruthenium(II)-based photosensitizer TLD1433, ($[Ru(bpy)(IP\text{-}TT)]^{2+}$ (IP-TT = 2-(2′,2″:5″,2‴-terthiophene)imidazo[4,5-*f*][1,10]phenanthroline),[16] has recently been approved for phase II clinical trial for nonmuscle invasive bladder cancer.[17] A ruthenium(III) antimetastatic agent BOLD-100 (Na[*trans*-$RuCl_4(Ind)_2$], where Ind = indazole)[18] is currently being explored in combination with cytotoxic FOLFOX chemotherapy for the treatment of solid tumors (colorectal, pancreatic, gastric, and cholangiocarcinoma).[19]

As described above, ruthenium derivatives have also been effective in breast cancer preclinical models[20] and most specifically in TNBCs,[13,20] with examples of ruthenium compounds efficacious in TNBC mice models[21−25] (including organometallics[22−25]). In this context, we reported in 2014 on iminophosphorane (IM)-containing cationic ruthenium(II) compounds coordinated through the nitrogen and oxygen atoms to the ruthenium center, as well as *p*-cymene and chloride ligands.[23,24] From the compounds studied, Ru-IM (**1** in Chart 1) containing chlorine as a counterion displayed high solubility in water ($H_2O$; 100 mg $mL^{-1}$) and had high stability as a solid (at least for 2 years) in a dimethyl sulfoxide (DMSO) solution (for months) and in $H_2O$ (half-life of 2.5 days). The preparation of **1** is relatively inexpensive compared to that of other metallodrugs, inhibitors, and antibody-based therapies. We showed that **1** is highly cytotoxic against several cell lines resistant to cisplatin including the TNBC cell line MDA-MB-231 (50-fold more cytotoxic than cisplatin). Compound **1** appears to follow a mechanism of action different from that of conventional platinum-based compounds. Not only does Ru-IM have a very weak interaction with DNA but also the cell death it induces does not depend on the p53 pathway. Additionally, we found **1** to be highly effective *in vivo*. We demonstrated that compound **1** (5 mg $kg^{-1}$ dose every 48 h for 28 days) was able not only to inhibit tumor growth but also to significantly decrease the tumor size (56%) in MDA-MB-231 xenograft-bearing NOD.CB17-Prkdc SCID/J mice. **1** displayed negligible systemic toxicity and a favored ruthenium tumor accumulation compared to other organs, with quick absorption into blood plasma and elimination after ca. 12 h.[23,24]

More recently, we have reported on the evaluation of this compound in a panel of TNBC cancer cell lines from different ethnic backgrounds, as well as against the National Cancer Institute (NCI) 60-cell-line panel.[26] Compound **1** was highly cytotoxic against most cancer types and cell lines. In addition, we reported that **1** induces apoptosis (G2/M arrest) and


https://doi.org/10.1021/acs.inorgchem.1c02929
Inorg. Chem. 2021, 60, 19152−19164

**Scheme 1. Synthesis of New IM Ligands 2a and 2b and Ru-IM Derivatives 3a and 3b**[a]

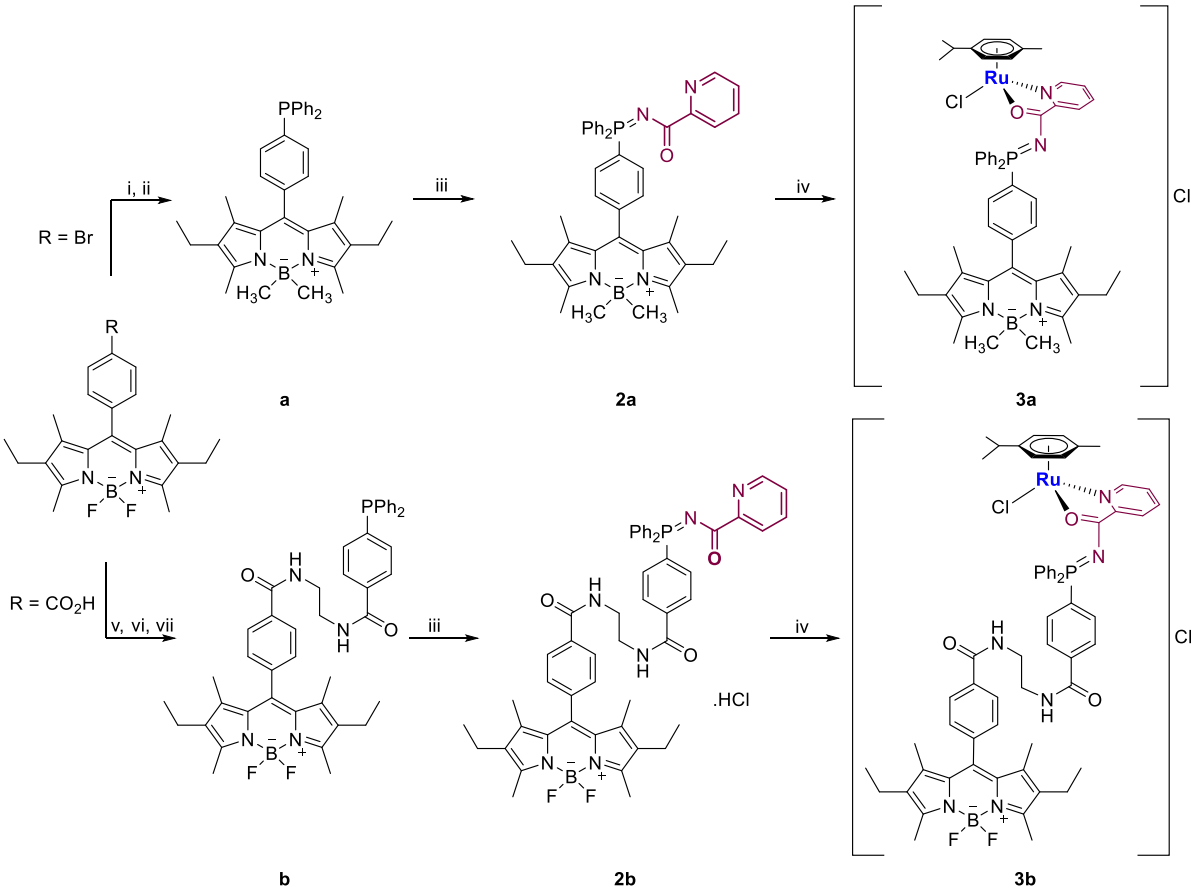


[a]Reaction conditions: (i) $CH_3Li$, THF, rt; (ii) $^nBuLi$, $PPh_2Cl$, $Et_2O$, −78 °C; (iii) pyridine-2-carbonyl azide, $CH_2Cl_2$ rt; (iv) $[(\eta^6\text{-}p\text{-cymene})Ru(\mu\text{-}Cl)Cl_2]_2$, acetone rt; (v) EDC·HCl, DMAP, NHS, $CH_2Cl_2$ rt; (vi) ethylenediammine, $CH_2Cl_2$, rt; (vii) $PPh_2$-COO-NHS, TEA, $CHCl_3$, 60 °C.

displays potential antimetastatic and antiangiogenic properties in two TNBC cell lines (MDA-MB-231 and HCC-1806) that are derived from patients with European and African ancestry, respectively. Preliminary proteomic assays point to a potential involvement of the PI3K/AKT pathway.[26]

Fluorophores based on the BODIPY core (4,4-difluoro-4-bora-3a,4a-diaza-*s*-indacene) are attractive dyes utilized for diverse applications including biomolecular labeling. These dyes have features that make them particularly appealing for this application, such as photochemical and chemical stability and high absorption coefficients and quantum yields. These fluorophores are excited, emit in the portion of the spectral region corresponding to the visible to near-IR, and display very short fluorescence lifetimes (on the order of nanoseconds), as well as weak triplet-state formation.[27−31] A number of synthetic routes (mild conditions) have been described to append a range of different substituents to the BODIPY core to tune the color, electronic, and solubility properties (for example, to generate water-soluble derivatives[32]). BODIPY-metal-based compounds with biomedical applications, with examples of optical imaging in living cells, have been reviewed.[33] BODIPY-phosphanes[34−36] have been described and utilized in the synthesis of metal-based compounds with potential theranostic applications [including ruthenium(II) compounds] as well as for intracellular localization studies.[34]

Here, we report on the synthesis and characterization of luminescent analogues of **1** by the incorporation of BODIPY or a BODIPY-modified fluorophore (4,4-dimethyl-4-bora-3a,4a-diaza-*s*-indacene) on the phosphane of the IM scaffold (compounds **3a** and **3b** in Chart 1) with the goal of studying their intracellular localization by fluorescence microscopy and gaining insight into potential targets and the mode of action of **1**.

## RESULTS AND DISCUSSION

**Synthesis and Characterization of IM-BODIPY Ligands and Ru-IM-BODIPY Analogues.** In order to incorporate the BODIPY scaffold in the IM ligand, two previously reported phosphanes containing BODIPY, 8-[(4-diphenylphosphino)phenyl]-4,4-dimethyl-1,3,5,7-tetramethyl-2,6-diethyl-4-bora-3a,4a-diaza-*s*-indacene (**a**)[35] and 4,4-difluoro-8-[4-[[2-[4-(diphenylphosphino)benzamido]ethyl]-carbamoyl]phenyl]-1,3,5,7-tetramethyl,2,6-diethyl,4-bora-3a,4a-diaza-*s*-indacene (**b**),[36] were used. Phosphane **a** was obtained by methylation of the fluorine atoms in the initial aryl bromide-containing BODIPY and further lithiation at low temperature, followed by the addition of chlorodiphenylphosphane[34] (Scheme 1, R = Br).

Phosphane **b** was obtained by the coupling of an aryldiphenylphosphane-activated ester and ethylenediamine-functionalized BODIPY obtained from the initial arylcarboxylic acid-containing BODIPY[36] (Scheme 1, R = $CO_2H$). Both phosphanes can react with pyridine-2-carbonyl azide in dry dichloromethane at room temperature (rt; Staudinger reaction, Scheme 1) to afford the new iminophosporane ligands as an


https://doi.org/10.1021/acs.inorgchem.1c02929
Inorg. Chem. 2021, 60, 19152−19164

air-stable light-orange powder (**2a**) and a dark-red crystalline solid (**2b**) in moderate yields (55−57%). The addtion of **2a** and **2b** IM-BODIPY ligands to $[(\eta^6\text{-}p\text{-cymene})\mathrm{Ru}(\mu\text{-Cl})\mathrm{Cl}]_2$[37] (Scheme 1), as previously described,[23,38] affords the cationic Ru-IM compounds containing BODIPY scaffolds as an air-stable orange crystalline solid (**3a**) and a bright-red powder (**3b**) in yields of 73 and 75%, respectively.

Spectroscopic (IR and NMR), elemental (CHN) analysis, and mass spectrometry data (see the Experimental Section and Supporting Information) confirm the structures proposed for IM ligands **2a** and **2b** and ruthenium compounds **3a** and **3b**. As reported before for Ru-IM complexes (Urriolabeitia et al.[38] and our laboratory[23,24]) in **3a** and **3b**, the IM chelating ligand coordinates to the ruthenium atom through the oxygen and nitrogen atoms to provide a fac-Cl,N,O arrangement. This fact is supported by IR spectroscopic data. The absorption (strong) due to $\nu_{CO}$ stretching at 1526 $cm^{-1}$ (**3a**) and 1537 $cm^{-1}$ (**3b**) is shifted to slightly lower frequencies with respect to that of the noncoordinated IM ligands at 1550 $cm^{-1}$ (**2a**) and 1539 $cm^{-1}$ (**2b**). The $^{31}P\{^1H\}$ NMR signals for **3a** and **3b** do not change much with respect to that of the free ligands **2a** and **2b**. Moreover, the structure of the ruthenium compound **3a** has been determined by X-ray analysis. This structure resembles that of $[(\eta^6\text{-}p\text{-cymene})\mathrm{Ru}(\kappa\text{-N,O-Ph}_3\mathrm{P{=}N\text{-}CO\text{-}2NC}_5\mathrm{H}_4)]\mathrm{PF}_6$ (analogue to **1** with a $PF_6^-$ anion)[23] and $[(\eta^6\text{-}C_6H_6)\mathrm{Ru}(\kappa\text{-N,O-Ph}_3\mathrm{P{=}N\text{-}CO\text{-}2NC}_5\mathrm{H}_4)]\mathrm{PF}_6$.[38]

The molecular structure for the cation of **3a** is depicted in Figure 1. Table 1 collects the selected bond lengths and angles.

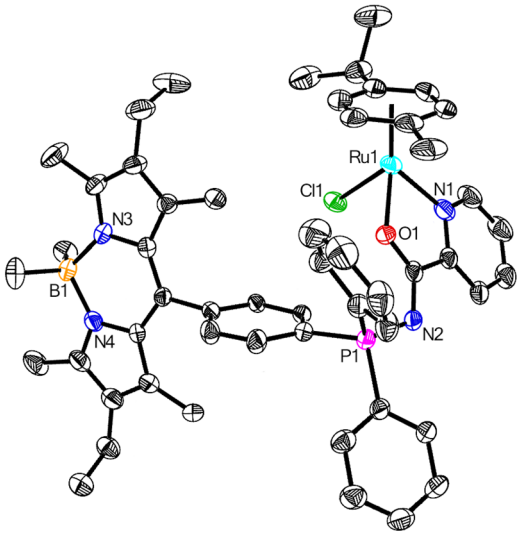


**Figure 1.** Molecular structure for the cation of **3a**.

The X-ray crystal structure analysis included one disordered molecule of pentane. The analysis confirms coordination of the IM-BODIPY ligand **2a** to the ruthenium atom in **3a** through the nitrogen and oxygen atoms as well as a resulting piano-stool structure. The distances between Ru−N [2.092(5) Å] and Ru−Cl [2.3823(14) Å] are near those reported for **1** of 2.095(4) and 2.3775(14) Å, respectively. The distance Ru−O for **3a** of 2.085(4) Å is shorter than that of 2.110(3) Å in **1**, which may indicate a slightly stronger bond. The average Ru−C distances (coordinated *p*-cymene) are very similar between the two compounds, and the angles O1−Ru1−N1 and N1−Ru1−Cl1 are slightly larger for **3a** than for **1**.

**Table 1. Select Bond Lengths [Å] and Angles [deg] for 3a**

| | | | |
|---|---|---|---|
| Ru1−O1 | 2.085(4) | N1−C1 | 1.355(8) |
| Ru1−N1 | 2.092(5) | C1−C2 | 1.380(10) |
| Ru1−C6 | 2.169(6) | N1−C5 | 1.356(8) |
| Ru1−C7 | 2.191(6) | C5−C16 | 1.487(8) |
| Ru1−C8 | 2.184(6) | N2−C16 | 1.313(7) |
| Ru1−C9 | 2.176(6) | P1−N2 | 1.630(5) |
| Ru1−C10 | 2.156(6) | N3−B1 | 1.586(8) |
| Ru1−C11 | 2.183(6) | N4−B1 | 1.584(8) |
| Ru1−Cl1 | 2.3823(14) | B1−C61 | 1.601(9) |
| O1−C16 | 1.276(6) | B1−C60 | 1.619(9) |
| O1−Ru1−N1 | 77.06(17) | N1−Ru1−Cl1 | 84.01(14) |
| O1−Ru1−Cl1 | 85.63(10) | | |

Solubility and lipophilicity are the two key physicochemical aspects that may predict the absorption and/or cellular uptake of a molecule. We investigated these two properties to obtain a glimpse of the complexes' potential pharmacodynamic profiles.[39] The molecular structure, among other factors, affects the solubility of the compounds, and therefore the solubility in $H_2O$ of **1** was altered by replacement of the IM by IM-BODIPY ligands **2a** and **2b**. Thus, ruthenium compound **3a** presented a low solubility in $H_2O$ (0.2 mg $mL^{-1}$), or a 500-fold decrease with respect to that of compound **1** (100 $mgL^{-1}$), while **3b** was insoluble in $H_2O$.

The lipophilicity of the ruthenium compounds was evaluated by liquid chromatography (LC/MS) in a 1:1 mixture of 1-octanol and water (values in Table 2; see the plots and details of the standard curves in Table S2 and Figure S21).

**Table 2. log *P* of Ru-IM Complexes[a]**

| | 1 | 3a | 3b |
|---|---|---|---|
| log *P* | 1.45 ± 0.02 | 2.20 ± 0.27 | 3.21 ± 0.08 |

[a]log *P* was performed in a 1:1 mixture of 1-octanol and phosphate-buffered saline. Data are shown as the mean ± standard deviation. Experiments were carried out in triplicate.

We observed that the lipophilicity of the compounds increases with the bulk of the IM ligand as the solubility decreases. Thus, log *P* of the bulkiest complex, **3b**, was 3.21, while **3a** showed a log *P* value of 2.20. Both complexes presented low aqueous solubility, as could be predicted by the general solubility equation of Yalkowsky and Banerjee.[40] The lipophilicity of compound **1** was 1.45, which is in accordance with the theoretical values of the ruthenium(II) arene complexes reported previously.[41] However, compound **1** is extremely soluble in $H_2O$ (as mentioned before). It is crucial to consider that the solubility of a compound is affected not only by its lipophilicity but also by its size and crystal lattice energy. It is also important to consider that these Ru-IM compounds are ionizable, and therefore the distribution of the species might be impacted by the pH.

The ruthenium complexes containing BODIPY (**3a** and **3b**) are stable for at least 2.5 weeks in a DMSO-$d_6$ solution as studied by $^{31}P\{^1H\}$ and $^1H$ NMR spectroscopy (see the spectra in Figures S15−S20). The low solubility in $H_2O$ prevented a study by NMR spectroscopy in $D_2O$ or a DMSO-$d_6$/$D_2O$ mixture. We had reported that the half-life for **1** in $D_2O$ was 2.5 days. In its $^{31}P\{^1H\}$ and $^{13}C\{^1H\}$ NMR spectra, signals attributable to a cyclometalated species were observed.


https://doi.org/10.1021/acs.inorgchem.1c02929
Inorg. Chem. 2021, 60, 19152−19164

Table 3. Quantum Yields (Φ), Molar Extinction Coefficients ($\varepsilon$), and Brightness ($B$) of Phosphane Ligands (a and b), IM-BODIPY Ligands (2a and 2b), and Ru-IM-BODIPY Complexes (3a and 3b)[a]

| | phosphane **a** | IM **2a** | Ru-IM **3a** | phosphane **b** | IM **2b** | Ru-IM **3b** |
|---|---|---|---|---|---|---|
| $\lambda_{abs}$(nm) | 510 | 511 | 511 | 524 | 524 | 524 |
| $\lambda_{em}$(nm) | 523 | 526 | 528 | 538 | 538 | 538 |
| Φ[b] (%) | 28(2) | 21(2) | 0.9(1) | 57(4) | 54(4) | 14(1) |
| $\varepsilon \times 10^4$ ($M^{-1}$ $cm^{-1}$) | 6.04(8) | 5.3(1) | 6.03(7) | 6.9(23) | 5.2(1) | 6.55(6) |
| $B \times 10^4$ ($M^{-1}$ $cm^{-1}$)[c] | 1.7(1) | 1.1(1) | 0.053(6) | 3.9(3) | 2.8(2) | 0.93(8) |

[a]All measurements were conducted at least in triplicate in 1:1 aerated acetonitrile/water at 25 °C. The numbers in parentheses correspond to the uncertainty in the last significant figure. [b]The samples were excited at their corresponding absorption maxima. The relative luminescence quantum yields were determined using fluorescein as a reference; Φ = 0.93 in 0.1 M NaOH; $\lambda_{exc}$ = 490 nm. [c]The brightness was calculated as the product of $\varepsilon$ and Φ.

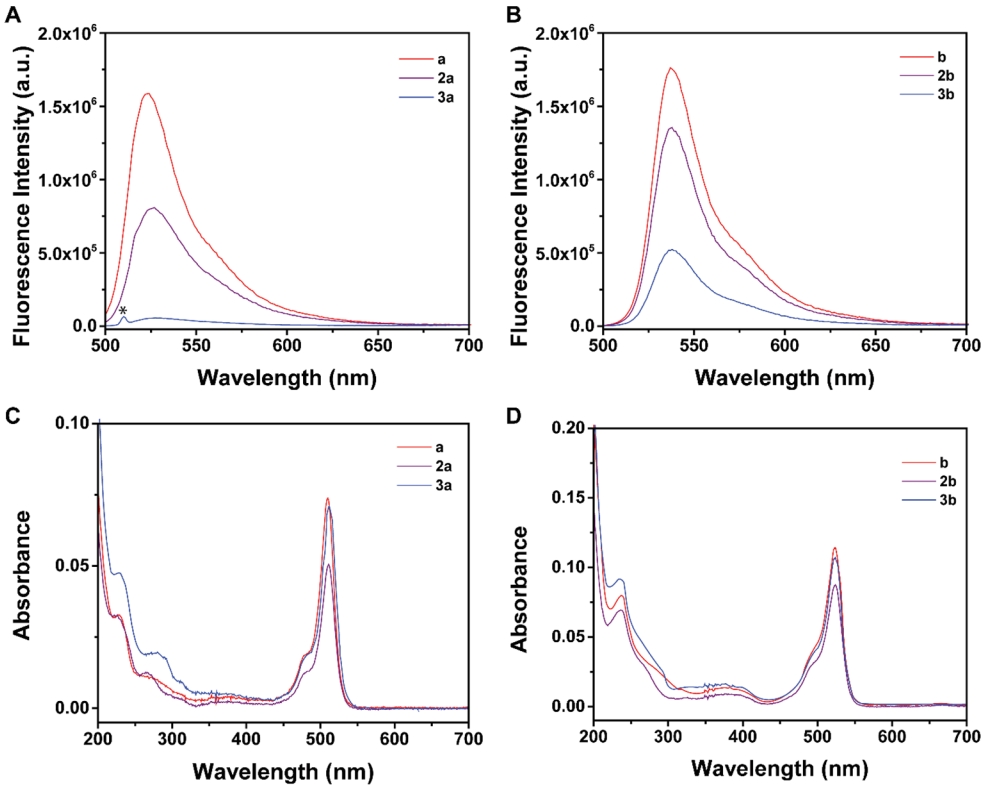


**Figure 2.** (A and B) Fluorescence emission ($\lambda_{exc}$ = 524 nm) and (C and D) absorption spectra of compounds **a**, **2a**, and **3a** (A and C) and compounds **b**, **2b**, and **3b** (B and D) in 1:1 acetonitrile/water at 25 °C. The scattering peak from the excitation light is marked with an asterisk.

Compound **1** was stable for several weeks in DMSO-$d_6$.[23] The stability of compounds **3a** and **3b** was assessed by UV−Vis spectroscopy in acetonitrile/$H_2O$ and in acetonitrile/DMEM media solutions (1:1 ratio) over time at 25 °C (see Figure S23 in SI.) The compounds seem to be quite stable after incubation for 72 h (especially **3a**). The intensity decrease of the signal for compound **3a** at $\lambda_{max}$ = 511 nm is almost negligible (<2%) for the two solvent systems after 24 or 72 h. In the case of **3b**, the intensity of the signal at $\lambda_{max}$ = 524 nm decreases at 9−10% after 24 h incubation in the acetonitrile/$H_2O$ and in acetonitrile/DMEM media solutions, while after 72 h this decrease is about 11% in acetonitrile/$H_2O$ and 17% in the acetonitrile/DMEM media solution.

**Photophysical Properties of the IM-BODIPY Ligands and Ru-IM BODIPY Analogues.** The photophysical data were collected for the IM-BODIPY ligands (**2a** and **2b**) and Ru-IM-BODIPY analogues (**3a** and **3b**) in 1:1 aerated acetonitrile/water (Table 3). The relative luminescence quantum yield Φ was calculated using eq 1 (see the Experimental Section).

The previously described phosphanes **a** and **b** were also evaluated for comparison purposes. It had been reported that these phosphanes display a profile typical of BODIPY fluorophores, with absorption maxima at either 513 nm in dry degassed THF (**a**)[35] or 526 nm in $H_2O$ (**b**)[36] which are very similar to those reported here for **a** (510 nm) and **b** (524 nm) in 1:1 acetonitrile/water. In the same solvent, the phosphane ligands exhibit fluorescence emission bands at 523 and 538 nm for **a** and **b**, respectively (Figure 2). The emission wavelengths do not change much for the IM-BODIPY ligands **2a** and **2b** or the Ru-IM complexes **3a** and **3b** (Figure 2 and Table 3).

The emission quantum yields of phosphanes **a** and **b** (Φ = 28 and 57%, respectively) are not affected by incorporation into the IM scaffold [Φ = 21% (**2a**) and 54% (**2b**)]. The fluorescence of the IM-BODIPY ligands are, however, significantly quenched by coordination to the ruthenium(II)


https://doi.org/10.1021/acs.inorgchem.1c02929
Inorg. Chem. 2021, 60, 19152−19164

Table 4. Half-Maximum Inhibitory Concentrations ($IC_{50}$, $\mu$M) of the IM-BODIPY Ligands and Ru-IM-BODIPY Compounds[a]

| | compound | | | | |
|---|---|---|---|---|---|
| cell line | Ru-IM (**1**) | IM-BODIPY (**2a**) | IM-BODIPY (**2b**) | Ru-IM-BODIPY (**3a**) | Ru-IM-BODIPY (**3b**) |
| MDA-MB-231 | 2.72 ± 0.11 | 134.95 ± 16.5 | >250 | 68.23 ± 8.2 | 116.3 ± 13.3 |
| MCF10a | 2.52 ± 0.48 | 33.7 ± 9.5 | >250 | 66.86 ± 13.4 | 72.97 ± 10.6 |
| IMR-90 | 30.4 ± 6.4 | 122.65 ± 3.8 | >250 | 60.33 ± 18.5 | 179.6 ± 8.77 |

[a]Following 72 h of incubation, a MTT reagent was used to quantify the values. All compounds were dissolved in 0.1% DMSO. The results are expressed as the mean ± standard deviation of experiments in triplicate.

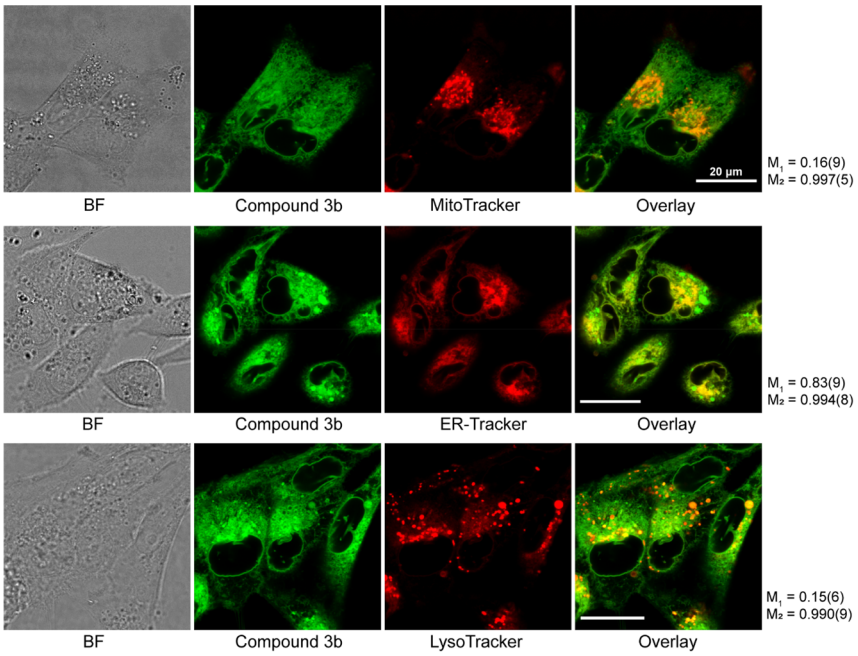


**Figure 3.** Confocal microscopy images of live MDA-MB-231 cells treated with Ru-IM-BODIPY compound **3b** (10 $\mu$M) and MitoTracker Deep Red FM (top), ER-Tracker Red (middle), and LysoTracker Deep Red (bottom). Images acquired in the range of emission of the BODIPY dye are pseudocolored in green, whereas images of the organelle stains are pseudocolored in red. The image overlay of both fluorescence channels shows the colocalization of compound **3b** and organelle markers. Manders' colocalization coefficient $M_1$ reflects the fraction of the total signal emitted by **3b** that overlaps with the organelle tracker, whereas M2 reflects the fraction of the total signal of the organelle marker that overlaps with that of compound **3b**. Values in parentheses represent the uncertainty in the last significant figure.

centers [$\Phi$ = 0.9% (**3a**) and 14% (**3b**)]. The quenching of fluorescence in ruthenium(II) compounds containing BODIPY moieties has been previously described[36,42] and is attributed to the promotion of triplet states[42] and/or photoinduced electron transfer.[43] Decreasing the electronic communication between the fluorophore and ruthenium center through an aliphatic spacer ameliorates the effect, and thus the brightness of **3b** is higher than that of **3a** and sufficient enough to allow visualization in living cells.

**Cellular Viability, Intracellular Localization, and Cellular and Organelle Uptake.** The cytotoxicity of the new IM-BODIPY ligands (**2a** and **2b**) and Ru-IM-BODIPY compounds (**3a** and **3b**) as well as that of parent **1** was evaluated in a TNBC cell line (MDA-MB-231), nontumorigenic breast cells (MCF10a), and lung fibroblasts (IMR-90). **1** was tested for comparative purposes. The cell lines were incubated with the above-described compounds for 72 h. The cell growth inhibition caused by the compounds was evaluated using MTT cell viability assay (see the Experimental Section). The results are summarized in Table 4.

IM ligand **2b** is not toxic to any of the cell lines studied, and the cytotoxicity of **2a** in the TNBC cell line is low (>100 $\mu$M). The Ru-IM-BODIPY analogues are all cytotoxic to the TNBC cell line, although the cytotoxicity decreases with the incorporation of the BODIPY motif in the IM ligand compared to the unmodified **1**. Compound **3a** is ca. 25-fold less toxic than **1**, while **3b** is 43-fold less toxic. Compounds **3b** and especially **1** are less toxic to noncancerous lung fibroblasts but are toxic to nonmalignant breast cancer cell lines MCF10a (an effect that we[26] and others[44] have also observed for a variety of metal-based compounds in this cell line, including compounds like **1**, which have low or no systemic toxicity *in vivo* in mice models).

Ruthenium compounds have shown varied preferential localization in different cellular compartments and organelles, mostly in nuclear,[45] lysosomal,[46] and mitochondrial[47] compartments. Intracellular localization studies with ruthenium compounds that incorporate BODIPY ligands in their structure have been reported,[36,48−52] as well as studies to assess cellular uptake.[53] Ruthenium(II) *p*-cymene compounds with chelating O,O[49] and N,O[50] ligands containing BODIPY have accumulated preferentially in mitochondria, while with pyridine[48] and bipyridyl[52] BODIPY-modified ligands, accumulation in both mitochondria and the endoplasmic reticulum was observed. Metallorectangles based on ruthenium(II) *p*-cymene derivatives with BODIPY-modified polypyridyl ligands were shown


https://doi.org/10.1021/acs.inorgchem.1c02929
Inorg. Chem. 2021, 60, 19152−19164

to have different preferential accumulation in cellular compartments depending on the type of cancer cell line.[49] Thus, in breast (MCF-7) and brain (U87) cell lines, these compounds accumulated in the cytoplasm, whereas in HeLa cell lines, they accumulated in the nuclei preferentially.[49] The ruthenium(II) *p*-cymene derivative with phosphane **b** was reported to bind nonspecifically to biological membranes in a way similar to that of free phosphane **b**.[36]

We performed fluorescence microscopy studies to visualize the uptake and distribution of Ru-IM-BODIPY compound **3b** in MDA-MB-231 cells (Figures 3 and S22). The compound is taken up by the cells, as revealed by the BODIPY-derived luminescence signal detected in different intracellular compartments, including the cytosol and organelles. Colocalization analysis with commercial organelle markers (Figures 3 and S22) points to accumulation of the ruthenium-BODIPY complex in the endoplasmic reticulum, mitochondria, and lysosomes. Specifically, Manders' colocalization coefficients,[54] $M_1$ = 0.83(9) and $M_2$ = 0.994(8) for compound **3b** and ER-Tracker Red, respectively, indicate that 83 ± 9% of the total luminescence signal emitted by compound **3b** coincides with areas stained by the ER marker. Similar analysis conducted in cells stained with Mitotracker Deep Red and Lysotracker Deep Red revealed 16 ± 9% of the total signal localized in mitochondria and 15 ± 6% in lysosomes. Additionally, staining of the nuclear envelope was observed with compound **3b**, although no significant signal was detected from the main body of the organelle.

Because the inclusion of the BODIPY motif may alter the behavior of Ru-IM-BODIPY analogues with respect to **1** (and we observed much higher lipophilicity with lower cytotoxicity for **3b**), we studied the accumulation and distribution in cytosol/organelles of ruthenium in TNBC MDA-MB-231 cells treated with **1** and **3b** by inductively coupled plasma optical emission spectrometry (ICP-OES), as summarized in Figure 4.

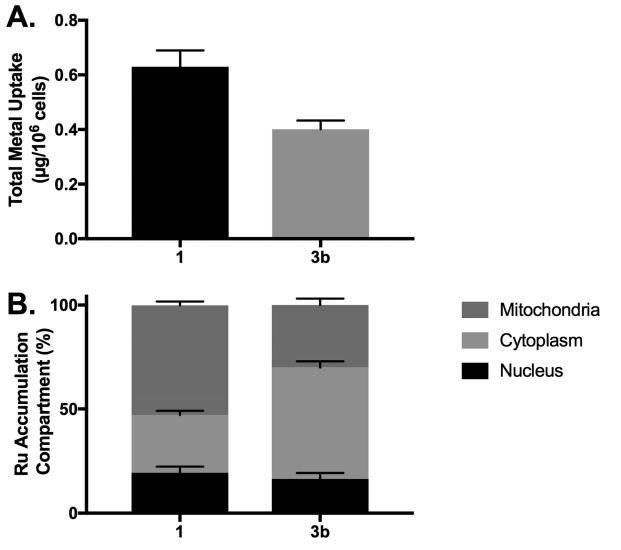


**Figure 4.** Ruthenium cellular uptake in MDA-MB-231 cells as determined by ICP-OES analysis. (A) Intracellular accumulation and (B) subcellular distribution of MDA-MB-231 cells treated with **1** or **3b** (2 μM, 2 h). The ruthenium uptake in the mitochondrial, cytoplasmic, and nuclear subcellular fractions are expressed as a proportion of the total ruthenium levels. The values represent the mean of at least two independent experiments, and error bars indicate the standard deviation.

The total ruthenium uptake of compounds **1** and **3b** by MDA-MB-231 cells was 83.8% and 64.3%, respectively, which was further analyzed through subcellular fractionation of the mitochondrial, nuclear, and cytoplasmic compartments to compare with the confocal microscopy results. While both compounds had similar localization in the nuclear compartment (compound **1**, 19.4%; compound **3b**, 16.4%), compound **1** showed 27.7% cytoplasmic accumulation and 52.7% mitochondrial accumulation, while compound **3b** had 53.5% cytoplasmic and 30.1% mitochondrial accumulation. We recently reported the cellular uptake of **1** in MDA-MB-231 at 75%. We utilized a fractionation kit for mitochondria and cytosol, where we observed an almost 50:50 ratio in the ruthenium content.[26] The study we present here is more complete.

The lipophilicity of small molecules is generally correlated to their cytotoxicity (the higher their lipophilicity, the better the cellular uptake and the higher their cytotoxicity). However, there is more complexity for metal-based cations. Factors such as the type of cellular uptake in effect (passive diffusion, transport proteins, or endocytosis)[55] or the potential interaction with serum proteins[56] may decrease the cellular uptake and cytotoxicity of compounds with higher lipophilicity in cell-based assays. In our case, **1** is highly soluble in $H_2O$ and less lipophilic than **3b** (insoluble in $H_2O$), but it displays a higher cellular uptake and much higher cytotoxicity than **3b**. Further studies on the mechanism of cellular uptake for compound **1** will be undertaken in the future.

Importantly, the results of ICP-OES are consistent with the results of image analysis for compound **3b** because they reveal greater ruthenium accumulation in the cytoplasmic fraction, including the endoplasmic reticulum and lysosomes, and smaller percentage accumulation in mitochondria and the nucleus. It should be noted that the percentage of the luminescence signal in an organelle quantified by Manders' coefficients is influenced not only by the concentration of the luminophore in the given compartment but also by the area occupied by the organelle in the cell image rather than the mass fraction of the whole cell. Accordingly, luminescence and ICP-OES analyses are not anticipated to provide the same numerical results, although they reveal similar trends. Microscopy analysis, however, provides greater resolution than typical fractionation studies, in some cases even at the suborganelle level. For compound **3b**, for example, microscopy reveals that the ruthenium detected in the nuclear fraction is mainly accumulated in the perinuclear membranes and not in the lumen of the organelle, where it could interact with nuclear DNA.

Last, because of the preferential ruthenium accumulation observed in the mitochondria for **1** by ICP-OES, we performed an assay to evaluate the possible production of reactive oxygen species (ROS; Figure 5). ROS generation is a measure of the oxidative damage in the cell that involves the production of superoxide, a byproduct usually associated with mitochondrial metabolism.[57] Several cellular functions require the production of moderate levels of ROS (including gene expression). In cancer cells, the production of ROS is amplified, but it is usually quenched by antioxidant pathways (although a moderate increase of the levels may promote tumor growth and metastatic processes). ROS are, however, known to trigger programmed cell death, and the modulation of ROS can be exploited as a strategy to develop anticancer therapeutics.[58]


https://doi.org/10.1021/acs.inorgchem.1c02929
Inorg. Chem. 2021, 60, 19152−19164

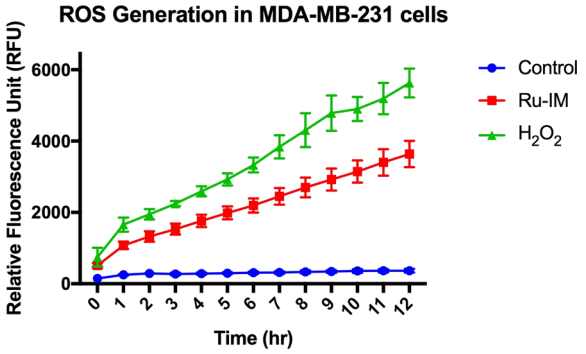


**Figure 5.** ROS generation in MDA-MB-231 cells. Cells were stained with ROS-detection dye DCF-DA and monitored over 12 h in a kinetic study. A comparison between the negative control (stained cells with no treatment) and the treatment with compound **1** ($IC_{50}$ value) shows a significant increase in ROS production in the presence of **1**, with known ROS generator $H_2O_2$ (1 mM) acting as a positive control. All data presented are expressed as the mean ± standard deviation. All samples were completed as three independent experiments.

ROS production in MDA-MB-231 cells exerted by **1** was measured using the fluorogenic marker dichlorodihydrofluorescein diacetate (DCF-DA), an oxidant-sensitive dye that converts to fluorescent species dicholorofluorescin (DCF) upon exposure to ROS. Over a 12 h kinetic study in MDA-MB-231 cells with nontreated cells as a negative control and 1 mM hydrogen peroxide ($H_2O_2$) as a positive control, **1** showed significant ($p < 0.001$) ROS generation upon treatment using an $IC_{50}$ value of the complex. This generation of ROS is comparable to that of other ROS-producing ruthenium complexes, such as ruthenium(II) cationic compounds like [Ru-ATZ]$^+$ containing cyclopentadienyl,[59] [Ru(Lap)-(dppm)$_2$]$PF_6$ containing lapachol,[60] and [RuNO(bpy)$_2$(4-pic)]$(PF_6)_3$ encapsulated in liposomes,[61] or that of anionic ruthenium(III) derivative BOLD-100 (currently in clinical trials).[62] For most anticancer drugs that generate ROS and provoke apoptosis, there is an activation of intrinsic pathways that involves an increase of the mitochondrial permeability, the release of activator factors, and the activation of caspases.[58] We have demonstrated that **1** exerts canonical or caspase-dependent apoptosis,[23,24,26] which is in accordance with the results described here (accumulation in the mitochondria and generation of ROS).

## CONCLUSIONS

In conclusion, we have synthesized two luminescent analogues (**3a** and **3b**) of a highly active organometallic ruthenium anticancer agent (**1**) by incorporation of the BODIPY fluorophore into the IM ligand coordinated to the ruthenium. As reflected by the emission quantum yields of compounds **3a** and **3b**, electronic decoupling of the fluorophore from the ruthenium center diminishes the luminescence quenching effect of the metal, resulting in overall better properties for imaging. Colocalization analysis with commercial organelle markers points to accumulation of the ruthenium-BODIPY complex in the endoplasmic reticulum, mitochondria, and lysosomes, which is further confirmed by ICP-OES analysis. As anticipated, we observed that the functionalization of **1** with the fluorophore has some effect on its lipophilicity, biological activity, and intracellular distribution. The ICP-OES data for **1** indicate a higher cellular uptake than fluorescently labeled **3b** and preferential accumulation in mitochondria with respect to other cytoplasmic organelles, although both compounds show similar nuclear accumulation. Despite these effects, fluorescence microscopy imaging of the emissive derivatives used in combination with orthogonal techniques for metal quantification can contribute to the building of a more complete picture of the cellular distribution of a compound, with spatial resolution superior to that of any one technique alone. The data reported here for compound **1** and its luminescent analogue will guide subsequent experiments to understand the mechanism(s) of this highly active compound and make further optimizations. A preliminary assay in MDA-MB-231 cells treated with **1** confirms a significant generation of ROS, which is in agreement with its preferential accumulation in the mitochondria and preliminary mechanistic data on the canonical or caspase-dependent nature of its apoptotic effects.

## EXPERIMENTAL SECTION

**Materials and Methods.** Air-free syntheses were performed using standard Schlenk-line techniques under a nitrogen atmosphere. A glovebox (MBraun MOD System) was used to store and manipulate air-sensitive compounds. Solvents were purified by use of a PureSolv purification unit from Innovative Technology, Inc. NMR spectra were recorded with a Bruker AV400 spectrometer ($^1$H NMR at 400 MHz, $^{13}$C{$^1$H} NMR at 100 MHz, $^{31}$P{$^1$H} NMR at 162 MHz, and $^{19}$F NMR at 376 MHz). Chemical shifts ($\delta$) are given in parts per million and coupling constants ($J$) in hertz using $CDCl_3$ or DMSO-$d_6$ as the solvent, unless otherwise stated. $^1$H and $^{13}$C{$^1$H} NMR resonances were measured relative to solvent peaks considering tetramethylsilane at 0 ppm; $^{31}$P{$^1$H} and $^{19}$F NMR were externally referenced to $H_3PO_4$ (85%) and $CFCl_3$, respectively. IR spectra (4000−500 cm$^{-1}$) were recorded on a Nicolet 6700 Fourier transform infrared spectrophotometer on the solid state (ATR accessory). Elemental analyses were performed on a PerkinElmer 2400 CHNS/O series II analyzer by Atlantic Microlab Inc. High-resolution electrospray ionization mass spectrometry (HR-ESI-MS) was performed on a Waters Q-Tof Ultima spectrometer. Theoretical isotopic distributions have been calculated using Molecular Weight Calculator, version 6.50. Absorption spectra were obtained using a Cary 100 UV−vis spectrophotometer ( Agilent Technologies) with 1 cm quartz cuvettes.

**Synthesis.** BODIPY-containing phosphanes 8-[(4-diphenylphosphino)phenyl]-4,4-dimethyl-1,3,5,7-tetramethyl-2,6-diethyl-4-bora-3a,4a-diaza-*s*-indacene (**a**)[35] and 4,4-difluoro-8-[4-[[2-[4-(diphenylphosphino)benzamido]ethyl]carbamoyl]phenyl]-1,3,5,7-tetramethyl,2,6-diethyl,4-bora-3a,4a-diaza-*s*-indacene (**b**),[36] pyridine-2-carbonyl azide,[63] [($\eta^6$-*p*-cymene)Ru($\mu$-Cl)Cl$_2$]$_2$,[37] $Ph_3P$═N-CO-2N$C_5H_4$ (IM),[64] and [($\eta^6$-*p*-cymene)Ru{$Ph_3P$═N-CO-2N$C_5H_4$)-$\kappa$-N,O}]Cl (Ru-IM, **1**)[23] were prepared as previously reported. Reaction solvents were purchased anhydrous from Fisher Scientific (BDH, ACS grade) and Sigma-Aldrich, used without further purification, dried in the Solvent Purification System (SPS) machine, and kept over molecular sieves (3 Å, beads, 4−8 mesh) or sodium. Deuterated solvents were purchased from Cambridge Isotope Laboratories, Inc., and kept over molecular sieves (3 Å, beads, 4−8 mesh).

**General Procedure for the Synthesis of BODIPY-$Ph_2P$═N-CO-2N-$C_5H_4$ (2a and 2b).** The reaction was performed under a nitrogen atmosphere. Pyridine-2-carbonyl azide (0.46 mmol) was dissolved in dichloromethane (10 mL). In a separate flask, the corresponding BODIPY-phosphane (**a** and **b**; 0.46 mmol) was dissolved in dichloromethane (10 mL) and added dropwise to pyridine-2-carbonyl azide via an addition funnel. The reaction was monitored by $^{31}$P{$^1$H} NMR. After no more starting phosphane was observed (~10 min), the solvent was removed under reduced pressure. The resulting solid was washed with hexane (3 × 5 mL) and further dried under reduced pressure to obtain a light-orange powder (**2a**) or a dark-red crystalline solid (**2b**).


https://doi.org/10.1021/acs.inorgchem.1c02929
Inorg. Chem. 2021, 60, 19152−19164

*2,6-Diethyl-4,4-dimethyl-1,3,5,7-tetramethyl-8-[4-[(P,P-diphenyl)[N-[1-(pyridin-2-yl)]methanoneyl]phosphinimidoyl]-phenyl]-4-bora-3a,4a-diaza-s-indacene (**2a**).* Yield: 57%. Anal. Calcd for $C_{43}H_{46}BN_4OP\cdot{}^3/_4$hexane·$^1/_4$LiBr: C, 74.77; H, 7.46; N, 7.34. Found: C, 74.90; H, 7.51; N, 7.26. HR-ESI-MS. Calcd: *m/z* 677.3575. Found: *m/z* 677.3610. $^1$H NMR ($CDCl_3$, 25 °C): $\delta$ 8.68 (d, *J* = 4.7 Hz, 1H, Ha), 8.26 (d, *J* = 7.9 Hz, 1H, Hb), 7.97 (d, *J* = 8.3 Hz, 1H, Ph), 7.94 (d, *J* = 8.2 Hz, 1H, Ph), 7.81−7.76 (m, 4H, Ph, He), 7.70 (td, *J* = 7.7 and 1.8 Hz, 1H, Hc), 7.52 (d, *J* = 7.4 Hz, 2H, Ph), 7.46−7.40 (m, 6H, Ph, He), 7.27 (ddd, *J* = 7.5, 4.7, and 1.3 Hz, 1H, Hd), 2.38 (s, 6H, Hf), 2.24 (q, *J* = 7.5 Hz, 4H, Hg), 1.21 (s, 6H, Hh), 0.91 (d, *J* = 7.5 Hz, 6H, Hi), 0.21 (s, 6H, Hj). $^{13}$C{$^1$H} NMR ($CDCl_3$, 25 °C): 175.5 (CO), 155.5 (C), 155.3 (C), 151.1 (4 × C), 149.3 (CH), 141.8 (C), 138.6 (C), 136.4 (CH), 133.9 (C), 133.8 (C), 133.4 (CH), 133.3 (2 × CH), 133.2 (2 × CH), 132.8 (CH), 132.5 (CH), 132.4 (CH), 129.4 (C), 129.3 (C), 128.8 (2 × CH), 128.7 (2 × CH), 128.6 (CH), 128.3 (CH), 127.8 (C), 127.3 (C), 124.9 (CH), 124.2 (CH), 17.4 (2 × $CH_2$), 14.6 (2 × $CH_3$), 14.4 (2 × $CH_3$), 12.1 (2 × $CH_3$), 1.0 (2 × $CH_3$). $^{31}$P{$^1$H} NMR ($CDCl_3$, 25 °C): 23.1. UV−vis (1:1 $CH_3CN/H_2O$, 25 °C): $\lambda_{max}$ = 511 nm ($\varepsilon$ = 53000 $M^{-1}$ $cm^{-1}$, *B* = 11000 $M^{-1}cm^{-1}$). IR ($cm^{-1}$): $\nu$ 2953 ($sp^3$ C−H), 2923 ($sp^3$ C−H), 1550 (C═O), 1107 (N═P).

*2,6-Diethyl-4,4-difluoro-1,3,5,7-tetramethyl-8-[4-[[2-[4-[(P,P-diphenyl)[N-[1-(pyridin-2-yl)]methanoneyl]phosphinimidoyl]-benzamido]ethyl]carbamoyl]phenyl]-4-bora-3a,4a-diaza-s-indacene (**2b**).* Yield: 55%. Anal. Calcd for $C_{51}H_{50}BF_2N_6O_3P\cdot HCl$: C, 67.22; H,5.64; N, 9.22. Found: C, 67.65; H, 5.57; N, 8.78. HR-ESI-MS. Calcd: *m/z* 875.3816. Found: *m/z* 875.3801. $^1$H NMR ($CDCl^3$, 25 °C): 8.60 (d, *J* = 4.8 Hz, 1H, Ha), 8.40 (bs, 1H, NH), 8.36 (d, *J* = 7.8 Hz, 1H, Hb), 8.16 (bs, 1H, NH), 7.98 (d, *J* = 8.3 Hz, 2H, Hj), 7.95 (dd, *J* = 8.0 and 2.7 Hz, 2H, Ph), 7.84−7.22 (m, 7H, Ph, Hc, He), 7.58 (td, *J* = 7.8 and 2.0 Hz, 2H, Ph), 7.47 (td, *J* = 7.9 and 3.2 Hz, 4H, Ph), 7.31 (ddd, *J* = 7.6, 4.8, and 1.2 Hz, 1H, Hd), 7.25 (d, *J* = 8.3 Hz, 2H, Hj), 3.68 (bs, 4H, Hp), 2.54 (s, 6H, Hf), 2.28 (q, *J* = 7.5 Hz, 4H, Hg), 1.18 (s, 6H, Hh), 0.97 (t, *J* = 7.5 Hz, 6H, Hi). $^{13}$C{$^1$H} NMR ($CDCl_3$, 25 °C): 175.3 (CO), 167.7 (CO), 167.6(CO), 155.1 (C), 154.9 (C), 154.1 (C), 149.0 (CH), 139.1 (C), 138.9 (C), 138.1 (C), 138.0 (C), 137.9 (C), 136.6 (CH), 134.4 (C), 133.3 (CH), 133.2 (3 × CH), 133.1 (2 × CH), 133.0 (CH), 132.8 (CH), 131.4 (C), 130.4 (2 × C), 130.4 (2 × C), 129.0 (2 × CH), 128.8 (2 × CH), 128.6 (2 × CH), 128.0 (2 × CH), 127.6 (CH), 127.5 (CH), 126.6 (2 × C), 125.2 (CH), 124.6 (CH), 41.5 ($CH_2$), 40.9 ($CH_2$), 17.1 (2 × $CH_2$), 14.6 (2 × $CH_3$), 12.5 (2 × $CH_3$), 11.8 (2 × $CH_3$). $^{31}$P{$^1$H} NMR ($CDCl_3$, 25 °C): 22.7. $^{19}$F NMR ($CDCl_3$, 25 °C): −145.66 (d, *J* = 30.1 Hz, 1F), −145.83 (d, *J* = 30.1 Hz, 1F). UV−vis (1:1 $CH_3CN/H_2O$, 25 °C): $\lambda_{max}$ = 524 nm ($\varepsilon$ = 52000 $M^{-1}$ $cm^{-1}$, *B* = 28000 $M^{-1}$ $cm^{-1}$). IR ($cm^{-1}$): $\nu$ 2932 ($sp^3$ C−H), 1539 (C═O), 1117 (N═P).

**General Procedure for the Synthesis of [($\eta^6$-*p*-Cymene)Ru-{(BODIPY-Ph$_2$P═N-CO-2N-C$_5$H$_4$)-$\kappa$-N,O}Cl]Cl (3a and 3b).** The corresponding IM-BODIPY ligand (**2a** and **2b**; 0.15 mmol) and [($\eta^6$-*p*-cymene)Ru($\mu$-Cl)Cl$_2$]$_2$ (0.065 mmol) were stirred in acetone (15 mL) for 2 h. The solvent was removed and the solid redissolved in 1−2 mL of chloroform. The ruthenium-BODIPY complexes were precipitated with cold diethyl ether (20 mL) and collected by filtration to afford an orange crystalline solid (**3a**) or a bright-red powder (**3b**).

*[($\eta^6$-p-Cymene)(2,6-diethyl-4,4-dimethyl-1,3,5,7-tetramethyl-8-[4-[(P,P-diphenyl)[N-[1-(pyridin-2-yl)]methanoneyl]-phosphinimidoyl]phenyl]-4-bora-3a,4a-diaza-s-indacene)-chlororuthenium(II)] Chloride (**3a**).* Yield: 73%. Anal. Calcd for $C_{53}H_{60}BCl_2N_4OPRu\cdot{}^3/_4CHCl_3$: C, 60.20; H, 5.71; N, 5.22. Found: C, 59.79; H, 5.90; N, 5.02. HR-ESI-MS. Calcd: *m/z* 947.3330. Found: *m/z* 947.3379. $^1$H NMR ($CDCl_3$, 25 °C): 9.94 (bs, 1H, Ha), 8.35 (d, *J* = 7.5 Hz, 1H, Hb), 8.03 (t, *J* = 7.5 Hz, 1H, Hc), 7.93−7.89 (m, 3H, Ph, He), 7.82−7.60 (m, 12H, Ph, Hd, He), 5.95 (bs, 2H, Hm), 5.74 (bs, 2H, Hn), 2.48 (s, 6H, Hf), 2.44−2.41 (m, 1H, Hl), 2.33 (q, *J* = 7.5 Hz, 4H, Hg), 2.07 (s, 3H, Ho), 1.30 (s, 6H, Hh), 1.11 (d, *J* = 6.8 Hz, 3H, Hk), 1.07 (d, *J* = 6.8 Hz, 3H, Hk), 1.01 (d, *J* = 7.5 Hz, 6H, Hi), 0.30 (s, 6H, Hj). $^{13}$C{$^1$H} NMR ($CDCl_3$, 25 °C): 178.5 (CO), 156.4 (CH), 151.6 (3 × C), 151.5 (C), 143.6 (C), 139.1 (CH), 137.6 (C), 133.9 (C), 133.6 (CH), 133.5 (CH), 133.4 (CH), 133.3 (CH), 133.2 (C), 133.1 (CH), 130.0 (CH), 132.9 (CH), 130.5 (C), 130.3 (C), 130.2 (CH), 129.7 (CH), 129.6 (CH), 129.5 (CH), 129.4 (CH), 128.4 (CH), 127.3 (C), 125.8 (C), 125.4 (CH), 125.2 (C), 124.8 (C), 124.3 (CH), 124.2 (CH), 102.5 (C), 97.8 (C), 83.8 (CH), 82.8 (CH), 82.5 (CH), 81.4 (CH), 30.9 (CH), 22.3 (CH), 22.0 ($CH_3$), 18.5 ($CH_3$), 17.7 (2 × $CH_2$), 14.7 (2 × $CH_3$), 14.4 (2 × $CH_3$), 12.2 (2 × $CH_3$), 1.0 (2 × $CH_3$). $^{31}$P{$^1$H} NMR ($CDCl_3$, 25 °C): 25.3. Found: *m/z* 947.3379. UV−vis (1:1 $CH_3CN/H_2O$, 25 °C): $\lambda_{max}$ = 511 nm ($\varepsilon$ = 60300 $M^{-1}$ $cm^{-1}$, *B* = 530 $M^{-1}$ $cm^{-1}$). IR ($cm^{-1}$): $\nu$ 2962 ($sp^3$ C−H), 1526 (C═O), 1110 (N═P).

*[($\eta^6$-p-Cymene)(2,6-diethyl-4,4-difluoro-1,3,5,7-tetramethyl-8-[4-[[2-[4-[(P,P-diphenyl)[N-[1-(pyridin-2-yl)]methanoneyl]-phosphinimidoyl]benzamido]ethyl]carbamoyl]phenyl]-4-bora-3a,4a-diaza-s-indacene)chlororuthenium(II)] Chloride (**3b**).* Yield: 78%. Anal. Calcd for $C_{61}H_{64}BCl_2F_2N_6O_3PRu\cdot{}^3/_2H_2O$: C, 60.65; H, 5.59; N, 6.96. Found: C, 60.66; H, 5.63; N, 6.68. HR-ESI-MS. Calcd: *m/z* 1145.3571. Found: *m/z* 1145.3480. $^1$H NMR ($CDCl_3$, 25 °C): 9.86 (bs, 1H, NH), 9.43 (bs, 1H, NH), 9.02 (d, *J* = 5.2 Hz, 1H, Ha), 8.68 (d, *J* = 8.0 Hz, 2H, Hj), 8.45 (d, *J* = 8.5 Hz, 2H, Ph), 8.42 (d, *J* = 7.5 Hz, 1H, Hb), 8.10 (t, *J* = 7.2 Hz, 1H, Hc), 7.84−7.54 (m, 13H, Ph, Hd, He), 7.24 (d, *J* = 8.0 Hz, 2H, Hj), 5.62 (d, *J* = 6.0 Hz, 1H, Hm), 5.70 (d, *J* = 6.0 Hz, 1H, Hm), 5.51 (d, *J* = 5.3 Hz, 1H, Hn), 5.47 (d, *J* = 5.5 Hz, 1H, Hn), 3.92 (bs, 2H, Hp), 3.82 (bs, 2H, Hp), 2.54 (s, 6H, Hf), 2.32−2.26 (m, 1H, Hl), 2.29 (q, *J* = 7.6 Hz, 4H, Hg), 2.00 (s, 3H, Ho), 1.23 (s, 6H, Hh), 1.08 (d, *J* = 6.8 Hz, 3H, Hk), 1.05 (d, *J* = 6.8 Hz, 3H, Hk), 0.98 (t, *J* = 7.6 Hz, 6H, Hi). $^{13}$C{$^1$H} NMR ($CDCl_3$, 25 °C): 177.4 (CO), 166.4 (2 × CO), 153.7 (CH), 152.8 (C), 152.6 (C), 152.3 (C), 140.2 (C), 140.1 (C), 139.9 (CH), 139.6 (C), 138.6 (C), 138.2 (C), 134.6 (C), 134.1 (CH), 133.6 (CH), 133.5 (CH), 132.9 (CH), 132.8 (CH), 132.7 (CH), 130.5 (C), 130.4 (2 × C), 130.1 (C), 129.7 (2 × CH), 129.6 (CH), 129.5 (2 × CH), 129.4 (CH), 129.1 (CH), 128.8 (CH), 128.7 (C), 128.1 (CH), 128.0 (CH), 127.4 (CH), 126.6 (2 × C), 125.0 (CH), 123.8 (CH), 122.9 (CH), 102.6 (C), 98.7 (C), 84.0 (CH), 83.9 (CH), 80.9 (CH), 80.7 (CH), 41.1 ($CH_2$), 39.4 ($CH_2$), 30.9 (CH), 22.3 ($CH_3$), 21.6 ($CH_3$), 18.3 ($CH_3$), 17.1 (2 × $CH_2$), 14.7 (2 × $CH_3$), 12.5 (2 × $CH_3$), 12.0 (2 × $CH_3$). $^{31}$P{$^1$H} NMR ($CDCl_3$, 25 °C): 26.8. $^{19}$F NMR ($CDCl_3$, 25 °C): −145.60 (d, *J* = 30.1 Hz, 1F), −145.77 (d, *J* = 30.1 Hz, 1F). UV−vis (1:1 $CH_3CN/H_2O$, 25 °C): $\lambda_{max}$ = 524 nm ($\varepsilon$ = 65500 $M^{-1}$ $cm^{-1}$, *B* = 9300 $M^{-1}$ $cm^{-1}$). IR ($cm^{-1}$): $\nu$ 2931 ($sp^3$ C−H), 1537 (C═O), 1116 (N═P).

**log *P*. Sample Preparation.** Organic (1-octanol) and aqueous (phosphate-buffered saline) phases were saturated and left for separation for 24 h prior to the study. A total of 10 $\mu$L each of **1**, **3a**, and **3b** stock solutions (10 mM in DMSO) were added to 990 $\mu$L of a 1:1 organic/aqueous mixture. Then, samples were vortexed for 1 h at 30 rpm, and the phases were isolated, transferred into high-performance liquid chromatography vials, and injected into the LC/MS system. log *P* was calculated in triplicate as the logarithm of [compound]organic phase/[compound]aqueous phase.

**LC/MS Injection.** A total of 1 $\mu$L of the sample was injected into the Agilent 6220 Accurate TOF LC/MS system equipped with a C18 column (Agilent Eclipse XDB-C18 5 $\mu$m, 4.6 × 150 mm). The mobile phases were (A) 5% acetonitrile and (B) 95% acetonitrile. Both phases contained 0.1% formic acid as the mobile phase additive. Data were acquired over 20 min at a flow rate of 0.5 mL $min^{-1}$ using the following gradient: (i) from 50% to 95% B (0−10 min); (ii) isocratic for 2 min, (iii) from 95% to 25% B (12−17 min); (iv) from 25% to 50% B (17−18 min); (v) isocratic for 2 min. The LC/MS data were analyzed by *MassHunter* software (version B.04.00; Agilent, Santa Clara, CA).

**X-ray Structure Determination.** The X-ray diffraction data for compound **3a** were collected on a Bruker X8 Kappa Apex II diffractometer using Mo K$\alpha$ radiation. Table S1 summarizes the data on the crystal, collection, and refinement parameters. The structure was solved using a dual-space method and standard difference map techniques and refined by full-matrix least-squares procedures on $F^2$ with *SHELXTL* (version 2017/1).[65] All hydrogen atoms were placed in calculated positions and refined with a riding model [$U_{iso}$(H) =


https://doi.org/10.1021/acs.inorgchem.1c02929
Inorg. Chem. 2021, 60, 19152−19164

1.2−1.5$U_{eq}$(C)]. The unit cell contained 18 pentane molecules, which were treated as a diffuse contribution to the overall scattering without specific atom positions by *SQUEEZE/PLATON*.[66]

**Spectroscopic Measurements.** All measurements were conducted at 25.0 ± 0.1 °C, maintained by a Quantum Northwest cuvette temperature controller. The acquisition of fluorescence spectra was completed with the use of a QuantaMaster 40 Photon Technology International spectrofluorometer equipped with a xenon lamp source, emission and excitation monochromators, an excitation correction unit, and a photomultiplier-tube detector. The emission spectra were corrected for the detector wavelength-dependent response. The excitation spectra were corrected for the wavelength-dependent lamp intensity. All aqueous solutions were prepared using deionized water having a resistivity of 18 MΩ·cm. Other solvents were obtained from commercial vendors and used as received.

**Determination of the Emission Quantum Yields.** The relative luminescence quantum yields were determined using 0.45−2.67 μM solutions of the BODIPY derivatives (phosphanes **a** and **b**, IM ligands **2a** and **2b**, and ruthenium compounds **3a** and **3b**) in 1:1 acetonitrile/water, exciting at the absorption maximum for each compound.[67] A solution of fluorescein in 0.1 M aqueous sodium hydroxide, with a reported quantum yield of 0.93 ± 0.02 upon excitation at 490 nm, was used as a standard.[68] Luminescence emission spectra were integrated from 518 to 700 nm for compounds **a**, **2a**, and **3a** and from 525 to 700 nm for compounds **b**, **2b**, and **3b**. The luminescence quantum yield $\Phi^i$ was calculated using eq 1:

$$\Phi^i = \Phi_F^s \frac{A^s}{A^i} \frac{F^i}{F^s} \left(\frac{n^i}{n^s}\right)^2 \quad (1)$$

where $\Phi_F^s$ is the quantum yield of the standard, $A^i$ and $A^s$ are the absorbances at the excitation wavelength of the compound and standard, respectively, $F^i$ and $F^s$ are the integrated luminescence intensities of the compound and standard, respectively, $n^i$ = 1.3472 is the calculated refractive index of the sample,[69] and $n^s$ = 1.333 is the refractive index of the standard.

**Cell Culture, Cell Viability, Imaging, and Cellular and Organelle Uptake.** *Cell Lines.* The human fetal lung fibroblast normal cell line (IMR-90) and TNBC MDA-MB-231 cells were purchased from the American Type Culture Collection (ATCC; Manassas, VA). The cells were cultured in Dulbecco's modified Eagle's medium (DMEM; Fisher Scientific, Hampton, NH) complemented with 10% fetal bovine serum (FBS), certified, heat inactivated, US origin (Fisher Scientific, Hampton, NH), 1% minimum essential media (MEM) nonessential amino acids (NEAA) (Fisher Scientific, Hampton, NH), and 1% penicillin−streptomycin (PenStrep) (Fisher Scientific, Hampton, NH). All cells were cultured in a humidified incubator at 37 °C under 5% $CO_2$ and 95% air.

*Cell Viability.* The viability was determined by MTT assay after treatment of the MDA-MB-231 and IMR-90 cells with compounds of interest. The cells were seeded into 96-well flat bottom microplates (Fisher Scientific, Waltham, MA) at a concentration of 5 × $10^3$ cells $well^{-1}$ in 100 μL of complete media and grown for 24 h at 37 °C under 5% $CO_2$ and 95% air in a humidified incubator. The cells were then dosed with all compounds ranging from 1 to 300 μM. After 72 h of drug exposure, 200 μL of a MTT reagent [5 mg of MTT or 3-(4,5-dimethylthiazol-2-yl)-2,5-diphenyltetrazolium bromide in 10 mL of the medium] was added to each well. Upon incubation for 3 h at 37 °C, 150 μL of the medium was removed and 100 μL of DMSO was added to each well, followed by up-and-down pipetting. Following a 15 min incubation, the absorbance was quantified with a BioTek Synergy Multimode microplate reader (BioTek Instruments, Inc., Winooski, VT) set at 550 nm. The percentage of surviving cells was calculated from the ratio of absorbance of treated to untreated cells. At least two independent experiments, each with triplicate measurements, were performed. *In vitro* $IC_{50}$ values were obtained after GraphPad Prism 8 nonlinear regression analysis.

**Cell Staining and Confocal Microscopy Protocols.** MDA-MB-231 cells were cultured in DMEM supplemented with 10% FBS at 37 °C in a 5% $CO_2$ humidified atmosphere. The cells were seeded in 35 mm glass bottom cell culture dishes (MatTek), and after ca. 48 h, the medium was replaced with DMEM containing 10 μM **3b**, in which the cells were incubated at 37 °C for 2 h. Organelle stain LysoTracker Deep Red (50 nM, Molecular Probes) or MitoTracker Deep Red FM (100 nM, Molecular Probes) was added in the final 30 min of incubation. Following washing with an imaging medium (phenol red-free DMEM), the cells were bathed in an imaging medium (2 mL) for image acquisition. For visualization of the endoplasmic reticulum, compound **3b** containing the medium was replaced with a prewarmed solution of ER-Tracker Red (500 nM, Molecular Probes) in Hank's Balanced Salt Solution with calcium and magnesium (HBSS/Ca/Mg) and incubated at 37 °C for 30 min. The cells were washed with warm HBSS/Ca/Mg and bathed in the same solution for image acquisition. Fluorescence imaging was performed on a Leica TCS SP8 X laser confocal microscope equipped with GaAsP hybrid detectors, a tunable white-light laser source, and a Leica DFC310 FX digital color camera. For the green channel, excitation was conducted at $\lambda_{ex}$ = 524 nm and emission collected at $\lambda_{em}$ = 530−570 nm. For the red channel, a combination of $\lambda_{ex}$ = 587 nm and $\lambda_{em}$ = 600−630 nm was used for the ER-Tracker and $\lambda_{ex}$ = 645 nm and $\lambda_{em}$ = 655−700 nm for the LysoTracker and MitoTracker. The microscope was operated with Leica LAS AF software. Image processing and colocalizations analyses were performed with *ImageJ 1.53c*.[69] After subtraction of the background, the regions of interest (ROIs) were defined around the cells by thresholding the signal in the green channel. Dead cells were removed manually from the ROIs, which were subsequently used for colocalization analysis using JACoP plugin.[70] For images of lysosomes and mitrochondria, respectively, the local background was derived from the median intensity in 16- and 46-pixel regions surrounding each pixel in the image of the organelle tracker. Upon background subtraction, colocalization in the ROIs was quantified using Manders' colocalization coefficients. In the JACoP interface, the thresholds were set so that the whole cell was visible in the green channel, the organelle of interest was visible in the red channel, and 500 rounds of Costes' randomization[71] were run. The Manders' colocalization coefficients values reported are the average of those obtained from at least three sets of images including a minimum of 35 cells each.

**Cell and Organelle Uptake.** To determine the ruthenium metal uptake in the MDA-MB-231 line, the cells were seeded onto a 6-well plate (Corning) at a density of 25 × $10^3$. Treatment with $IC_{20}$ concentration of **1** over 2 h was then completed. Following incubation, a subcellular fractionation buffer (20 mM HEPES, pH 7.4, 10 mM KCl, 2 mM $MgCl_2$, 1 mM EDTA, 1 mM EGTA, 1 mM DTT, protease inhibitor cocktail) was added, and the cell suspension was passed through a 27-gauge needle 10 times to lyse the cells. The cells were incubated on ice for 20 min and then centrifuged for 5 min at 720*g*. The supernatant was collected, which contained cytoplasm and mitochondrial components. The cell pellet, containing the nuclear fragment, was further passed 10 times through a 25-gauge needle with 500 μL of the fractionation buffer and then centrifuged at 720*g* for 10 min. The supernatant containing mitochondrial and cytoplasm components was centrifuged for 5 min at 10000*g*. The subsequent supernatant was collected as the cytoplasmic fraction, and the cell pellet was collected for the mitochondrial fragment. The nuclear and mitochondrial fractions were resuspended in TBS with 0.1% SDS and then sonicated to homogenize the lysates. The samples were then digested in a 1:2 ratio of a 70% nitric acid and 35% $H_2O_2$ mixture at 60 °C for 72 h. The samples were analyzed with a PerkinElmer Optima 7300 DV spectrometer and calibrated prior to use. The signals were monitored at a wavelength of 240.272. Biodistribution values are presented as the percent of the accumulated dose and were calculated by including the appropriate standards in triplicate samples. All data presented are expressed as the mean ± standard deviation.

**ROS Generation Assay.** MDA-MB-231 cells were plated in a 96-well plate with a density of 10000 cells $well^{-1}$. Following a 24 h seeding time, the cells were washed with Hank's Balanced Salt Solution (HBSS/Ca/Mg). A DCF-DA solution (100 μM in HBSS/Ca/Mg) was added to the cells and incubated at 37 °C at 5% $CO_2$ and 95% air for 30 min. Following incubation, the staining solution


https://doi.org/10.1021/acs.inorgchem.1c02929
Inorg. Chem. 2021, 60, 19152−19164

was washed off, and HBSS was added and further incubated for 30 min. Cells were then treated with negative (no treatment, stained) and positive (1 mM $H_2O_2$, known to produce ROS) controls and an $IC_{50}$ value of Ru-IM, and kinetic measurements were performed in 1 h increments over 12 h in a Biotek Synergy plate reader at a fluorescence excitation of 485 nm and an emission of 530 nm. All data presented are expressed as the mean ± standard deviation.

## ■ ASSOCIATED CONTENT

### Supporting Information

The Supporting Information is available free of charge at https://pubs.acs.org/doi/10.1021/acs.inorgchem.1c02929.

$^1H$, $^{13}C\{^1H\}$, $^{31}P\{^1H\}$, and $^{19}F$ NMR spectra ($CDCl_3$), solid FTIR spectra and LC/MS spectra ($ESI^+$) of compounds **2a**, **2b**, **3a**, and **3b**, NMR spectra in DMSO-$d^6$ ($^1H$ and $^{31}P\{^1H\}$) for stability studies of compounds **3a** and **3b** over time, crystal data, data collection, and refinement parameters for compound **3a**, limits of detection and quantification of ruthenium compounds **1**, **3a**, and **3b** as well as calibration curves (log *P* experiments), and scatter plots for colocalization analysis of **3b** in MDA-MB-231 cells with commercial organelle markers; UV−Vis spectra for **3a** and **3b** in acetonitrile/$H_2O$ and acetonitrile/DMEM media solutions (1:1) overtime (PDF)

### Accession Codes

CCDC 2089526 contains the supplementary crystallographic data for this paper. These data can be obtained free of charge via www.ccdc.cam.ac.uk/data_request/cif, or by emailing data_request@ccdc.cam.ac.uk, or by contacting The Cambridge Crystallographic Data Centre, 12 Union Road, Cambridge CB2 1EZ, UK; fax: +44 1223 336033.

## ■ AUTHOR INFORMATION


### Corresponding Authors

**Daniela Buccella** − *Department of Chemistry, New York University, New York, New York 10003, United States;* orcid.org/0000-0002-2266-9026; Email: dbuccella@nyu.edu

**Maria Contel** − *Department of Chemistry and Brooklyn College Cancer Center, Brooklyn College, The City University of New York, Brooklyn, New York 11210, United States; Biology Ph.D. Program, Chemistry, and Biochemistry Ph.D. Programs, The Graduate Center, The City University of New York, New York, New York 10016, United States;* orcid.org/0000-0002-9825-4441; Email: mariacontel@brooklyn.cuny.edu

### Authors

**Kirill Miachin** − *Department of Chemistry, Brooklyn College, The City University of New York, Brooklyn, New York 11210, United States*

**Virginia Del Solar** − *Department of Chemistry, Brooklyn College, The City University of New York, Brooklyn, New York 11210, United States;* Present Address: Cell and Gene Therapy Catapult, 12th Floor Tower Wing, Guy's Hospital, Great Maze Pond, London SE1 9RT, United Kingdom

**Elsy El Khoury** − *Department of Chemistry, New York University, New York, New York 10003, United States*

**Nazia Nayeem** − *Department of Chemistry and Brooklyn College Cancer Center, Brooklyn College, The City University of New York, Brooklyn, New York 11210, United States; Biology Ph.D. Program, The Graduate Center, The City University of New York, New York, New York 10016, United States*

**Anton Khrystenko** − *Department of Chemistry, Brooklyn College, The City University of New York, Brooklyn, New York 11210, United States*

**Patricia Appelt** − *Department of Chemistry, Brooklyn College, The City University of New York, Brooklyn, New York 11210, United States; Federal University of Paraná, 81540-990 Curitiba, Paraná, Brazil*

**Michelle C. Neary** − *Chemistry Department, Hunter College, The City University of New York, New York, New York 10021, United States;* orcid.org/0000-0003-2805-3668

Complete contact information is available at: https://pubs.acs.org/10.1021/acs.inorgchem.1c02929


### Author Contributions

The manuscript was written through contributions of all authors. All authors have given approval to the final version of the manuscript.

### Notes

The authors declare no competing financial interest.

## ■ ACKNOWLEDGMENTS

This work was supported by the National Institute of General Medical Sciences through Grant 2SC1GM127278-07A1 (to M.C.) and NCI through Grant R01CA217817 (to D.B.). We thank the Graduate Research Technology Initiative Fund Round 21 Supplement from CUNY for funds to purchase a plate reader (to M.C.). P.A. thanks the Brazilian Federal Agency for support and Evaluation Education (Capes) for a travel fellowship. We thank Dr. Ali Younes (Hunter College, The City University of New York) for help with the data analysis from ICP-OES experiments. We thank the Hunter College X-ray facility. The authors acknowledge the use of shared facilities provided through the Materials Research Science and Engineering Center program of the National Science Foundation under Award DMR-1420073.

## ■ REFERENCES

(1) https://www.wcrf.org/dietandcancer/breast-cancer-statistics/ (last checked on 09/16/2021).

(2) Kohler, B. A.; Sherman, R. L.; Howlader, N.; Jemal, A.; Ryerson, A. B.; Henry, K. A.; Boscoe, F. P.; Cronin, K. A.; Lake, A.; Noone, A.; Henley, S. J.; Eheman, C. R.; Anderson, R. N.; Penberthy, L. Annual Report to the Nation on the Status of Cancer, 1975−2011, Featuring Incidence of Breast Cancer Subtypes by Race/Ethnicity, Poverty, and State. *J. Natl. Cancer. Inst.* **2015**, *107*, djv048 [association of race/ethnicity, socioeconomic status, and breast cancer subtypes in the National Cancer Data Base (2010−2011)].

(3) Sineshaw, H. M.; Gaudet, M.; Ward, E. M.; Flanders, W. D.; Desantis, C.; Lin, C. C.; Jemal, A. Association of race/ethnicity, socioeconomic status, and breast cancer subtypes in the National Cancer Data Base (2010−2011). *Breast Cancer Res. Treat.* **2014**, *145*, 753−63.

(4) Patel, T. A.; Colón-Otero, G.; Bueno Hume, C.; Copland, J. A.; Pérez, E. A. Breast cancer in Latinas: gene expression, differential response to treatments, and differential toxicities in Latinas compared with other population groups. *Oncologist* **2010**, *15*, 466−475.

(5) Lara-Medina, F.; Pérez-Sánchez, V.; Saavedra-Pérez, D.; Blake-Cerda, M.; Arce, C.; Motola-Kuba, D.; Villarreal-Garza, C.; González-Angulo, A. M.; Bargalló, E.; Aguilar, J. L.; Mohar, A.; Arrieta, Ó. Triple-negative breast cancer in Hispanic patients: high prevalence,

poor prognosis, and association with menopausal status, body mass index, and parity. *Cancer* **2011**, *117*, 3658−3669.
(6) Gonçalves, H., Jr; Guerra, M. R.; Duarte Cintra, J. R.; Fayer, V. A.; Brum, I. V.; Bustamante Teixeira, M. T. Survival study of triple-negative and non-triple-negative breast cancer in a Brazilian cohort. *Clin. Med. Insights: Oncol.* **2018**, *12*, 1−10.
(7) Lehmann, B. D.; Jovanovic, B.; Chen, X.; Estrada, M. V.; Johnson, K. N.; Shyr, Y.; Moses, H. L.; Sanders, M. E.; Pietenpol, J. A. Refinement of triple-negative breast cancer molecular subtypes: Implications for neoadjuvant chemotherapy Selection. *PLoS One* **2016**, *11* (6), No. e0157368.
(8) Stover, D. G.; Bell, C. F.; Tolaney, S. M. Neoadjuvant and adjuvant chemotherapy considerations for triple-negative breast cancer. *Am. J. Hematol. Oncol.* **2016**, *12*, 6−12.
(9) Marra, A.; Viale, G.; Curigliano, G. Recent advances in triple negative breast cancer: the immunotherapy era. *BMC Med.* **2019**, *17*, 90.
(10) https://www.cancer.gov/about-cancer/treatment/clinical-trials/disease/breast-cancer/treatment (last checked on 09/16/2021).
(11) https://www.cancer.gov/news-events/cancer-currents-blog/2020/fda-sacituzumab-govitecan-triple-negative-breast-cancer (last checked on 09/16/2021).
(12) Islam, R.; Lam, K. W. Recent progress in small molecule agents for the targeted therapy of triple-negative breast cancer. *Eur. J. Med. Chem.* **2020**, *207*, 112812.
(13) Nayeem, N.; Contel, M. Exploring the potential of metallodrugs as chemotherapeutics for triple-negative breast cancer. *Chem. - Eur. J.* **2021**, *27*, 8891−8917.
(14) Coverdale, J. P. C.; Laroiya-McCarron, T.; Romero-Canelón, I. Designing ruthenium anticancer drugs: what have we learnt from the key drug candidates? *Inorganics* **2019**, *7*, 31.
(15) Adhireksan, Z.; Davey, G. E.; Campomanes, P.; Groessl, M.; Clavel, C. M.; Yu, H.; Nazarov, A. A.; Yeo, C. H. F.; Ang, W. H.; Droge, P.; Rothlisberger, U.; Dyson, P. J.; Davey, C. A. Ligand substitutions between ruthenium-cymene compounds can control protein versus DNA targeting and anticancer activity. *Nat. Commun.* **2014**, *5*, 3462.
(16) Monro, S.; Colon, K. L.; Yin, H. M.; Roque, J.; Konda, P.; Gujar, S.; Thummel, R. P.; Lilge, L.; Cameron, C. G.; McFarland, S. A. Transition metal complexes and photodynamic therapy from a tumor-centered approach: challenges, opportunities, and highlights from the development of TLD1433. *Chem. Rev.* **2019**, *119* (2), 797−828.
(17) https://clinicaltrials.gov/ct2/show/NCT03945162 (last checked on 09/16/2021).
(18) Neuditschko, B.; Legin, A. A.; Baier, D.; Schintlmeister, A.; Reipert, S.; Wagner, M.; Keppler, B. K.; Berger, W.; Meier-Menches, S. M.; Gerner, C. Interaction with ribosomal proteins accompanies stress induction of the anticancer metallodrug BOLD-100/KP1339 in the endoplasmic reticulum. *Angew. Chem., Int. Ed.* **2021**, *60* (10), 5063−5068.
(19) https://clinicaltrials.gov/ct2/show/NCT04421820 (last checked on 09/16/2021).
(20) Golbaghi, G.; Castonguay, A. Rationally designed ruthenium complexes for breast cancer therapy. *Molecules* **2020**, *25* (2), 265.
(21) Shen, J.; Kim, H. - C.; Wolfram, J.; Mu, C.; Zhang, W.; Liu, H.; Xie, Y.; Mai, J.; Zhang, H.; Li, Z.; Guevara, M.; Mao, Z. - W.; Shen, H. A liposome encapsulated ruthenium polypyridine complex as a theranostic platform for triple-negative breast cancer. *Nano Lett.* **2017**, *17*, 2913−2920.
(22) Mendes, N.; Tortosa, F.; Valente, A.; Marques, F.; Matos, A.; Morais, T. S.; Tomaz, A. I.; Gärtner, F.; García, M. H. In vivo performance of a ruthenium-cyclopentadienyl compound in an orthotopic triple negative breast cancer model. *Anti-Cancer Agents Med. Chem.* **2016**, *16*, 126−136.
(23) Frik, M.; Martínez, A.; Elie, B. T.; Gonzalo, O.; Ramírez de Mingo, D. R.; Sanaú, M.; Sánchez-Delgado, R.; Sadhukha, T.; Prabha, S.; Ramos, J. W.; Marzo, I.; Contel, M. *In vitro* and *in vivo* evaluation of water-soluble iminophosphorane ruthenium(II) Compounds. A potential chemotherapeutic agent for triple negative breast cancer. *J. Med. Chem.* **2014**, *57*, 9995−10012.
(24) Contel, M.; Marzo, I.; Frik, M.; Elie, B. T. Arene ruthenium (II) derivatives containing iminophosphorane ligands and their use in cancer therapy. U.S. Patent 9,555,049B2 (01/31/2017).
(25) Montani, M.; Pazmay, G. V. B.; Hysi, A.; Lupidi, G.; Pettinari, R.; Gambini, V.; Tilio, M.; Marchetti, F.; Pettinari, C.; Ferraro, S.; Iezzi, M.; Marchini, C.; Amici, A. The water soluble ruthenium(II) organometallic compound [Ru(p-cymene)(bis(3,5 dimethylpyrazol-1-yl)methane)Cl]Cl suppresses triple negative breast cancer growth by inhibiting tumor infiltration of regulatory T cells. *Pharmacol. Res.* **2016**, *107*, 282−290.
(26) Nayeem, N.; Yeasmin, A.; Cobos, S. N.; Younes, A.; Hubbard, K.; Contel, M. Investigation of the mechanisms of anticancer action of a Ru(II)-arene iminophosphorane compound in triple negative breast cancer cells. *ChemMedChem* **2021**, *16*, 3280−3292.
(27) Treibs, A.; Kreuzer, F. H. Di- and tri-pyrrylmethene complexes with di-fluoro boron. *Liebigs Ann. Chem.* **1968**, *718*, 208−223.
(28) Ziessel, R.; Ulrich, G.; Harriman, A. The chemistry of Bodipy: a new El Dorado for fluorescence tools. *New J. Chem.* **2007**, *31* (4), 496−501.
(29) Loudet, A.; Burgess, K. BODIPY dyes and their derivatives: syntheses and spectroscopic properties. *Chem. Rev.* **2007**, *107* (11), 4891−932.
(30) Ulrich, G.; Ziessel, R.; Harriman, A. The chemistry of fluorescent bodipy dyes: Versatility unsurpassed. *Angew. Chem., Int. Ed.* **2008**, *47* (7), 1184−1201.
(31) Kowada, T.; Maeda, H.; Kikuchi, K. BODIPY-based probes for the fluorescence imaging of biomolecules in living cells. *Chem. Soc. Rev.* **2015**, *44* (14), 4953−4972.
(32) Franke, J. M.; Raliski, B. K.; Boggess, S. C.; Natesan, D. V.; Koretsky, E. T.; Zhang, P.; Kulkarni, R. U.; Deal, P. E.; Miller, E. W. BODIPY fluorophores for membrane potential imaging. *J. Am. Chem. Soc.* **2019**, *141* (32), 12824−12831.
(33) Bertrand, B.; Passador, K.; Goze, C.; Denat, F.; Bodio, E.; Salmain, M. Metal-based BODIPY derivatives as multimodal tools for life sciences. *Coord. Chem. Rev.* **2018**, *358*, 108−124.
(34) Davies, L. H.; Stewart, B.; Harrington, R. W.; Clegg, W.; Higham, L. J. Air-stable, highly fluorescent primary phosphanes. *Angew. Chem., Int. Ed.* **2012**, *51* (20), 4921−4924.
(35) Davies, L. H.; Harrington, R. W.; Clegg, W.; Higham, L. J. $BR_2BodPR_2$: highly fluorescent alternatives to PPh3 and $PhPCy_2$. *Dalton Trans.* **2014**, *43*, 13485−13499.
(36) Tasan, S.; Zava, O.; Bertrand, B.; Bernhard, C.; Goze, C.; Picquet, M.; Le Gendre, P.; Harvey, P.; Denat, F.; Casini, A.; Bodio, E. BODIPY-phosphane as a versatile tool for easy access to new metal-based theranostics. *Dalton Trans.* **2013**, *42*, 6102−6109.
(37) Tönnemann, J.; Risse, J.; Grote, Z.; Scopelliti, R.; Severin, K. Efficient and rapid synthesis of chlorido-bridged half sandwich complexes of ruthenium, rhodium, and iridium by microwave heating. *Eur. J. Inorg. Chem.* **2013**, *2013*, 4558−4562.
(38) Aguilar, D.; Bielsa, R.; Soler, T.; Urriolabeitia, E. P. Cycloruthenated complexes from iminophosphoranes: synthesis, structure, and reactivity with internal alkynes. *Organometallics* **2011**, *30*, 642−648.
(39) Zeng, L.; Gupta, P.; Chen, Y.; Wang, E.; Ji, L.; Chao, H.; Chen, Z. S. The development of anticancer ruthenium(ii) complexes: from single molecule compounds to nanomaterials. *Chem. Soc. Rev.* **2017**, *46* (19), 5771−5804.
(40) Yalkowsky, S. H.; Banerjee, S. *Aqueous solubility: methods of estimation for organic compounds*; Marcel Dekker, Inc.: New York, 1992; p 142.
(41) Shweshein, K. S.; Andrić, F.; Radoičić, A.; Zlatar, M.; Gruden-Pavlović, M.; Tešić, Z.; Milojković-Opsenica, D. Lipophilicity assessment of ruthenium(II)-arene complexes by the means of reversed-phase thin-layer chromatography and DFT calculations. *Sci. World J.* **2014**, *2014*, 862796.
(42) Galletta, M.; Puntoriero, F.; Campagna, S.; Chiorboli, C.; Quesada, M.; Goeb, S.; Ziessel, R. Absorption spectra, photophysical

properties, and redox behavior of ruthenium(II) polypyridine complexes containing accessory dipyrromethene−$BF_2$ chromophores. *J. Phys. Chem. A* **2006**, *110*, 4348−4358.
(43) Juris, A.; Balzani, V.; Barigelletti, F.; Campagna, S.; Belser, P.; Von Zelewsky, A. Ru(II) polypyridine complexes: photophysics, photochemistry, electrochemistry, and chemiluminescence. *Coord. Chem. Rev.* **1988**, *84*, 85−277.
(44) Mao, Z.-W.; Muhammad, N.; Cai-Ping, T.; Nasreen, S. Redirecting cisplatin and doxorubicin to mitochondria affords highly effective platinumIV prodrug against triple negative breast cancer. *Chem. - Asian J.* **2021**, *16*, 2276−2279.
(45) Zhao, X.; Li, L.; Yu, G.; Zhang, S.; Li, Y.; Wu, Q.; Huang, X.; Mei, W. Nucleus-enriched ruthenium polypyridine complex acts as a potent inhibitor to suppress triple-negative breast cancer metastasis *in vivo*. *Comput. Struct. Biotechnol. J.* **2019**, *17*, 21−30.
(46) Cao, W.; Zheng, W.; Chen, T. Ruthenium polypyridyl complex inhibits growth and metastasis of breast cancer cells by suppressing FAK signaling with enhancement of TRAIL-induced apoptosis. *Sci. Rep.* **2015**, *5*, 9157.
(47) Ratanaphan, A.; Nhukeaw, T.; Hongthong, K.; Dyson, P. J. Differential cytotoxicity, cellular uptake, apoptosis and inhibition of BRCA1 expression of BRCA1-defective and sporadic breast cancer cells induced by an anticancer ruthenium (II)-arene compound, RAPTA-EA1. *Anti-Cancer Agents Med. Chem.* **2017**, *17*, 212−220.
(48) Wang, T.; Hou, Y.; Chen, Y.; Li, K.; Cheng, X.; Zhou, Q.; Wang, X. Two novel BODIPY−Ru(ii) arene dyads enabling effective photo-inactivation against cancer cells. *Dalton Trans.* **2015**, *44*, 12726−12734.
(49) Gupta, G.; Das, A.; Ghate, N. B.; Kim, T.; Ryu, J. Y.; Lee, J.; Mandal, N.; Lee, C. Y. Novel BODIPY-based Ru(ii) and Ir(iii) metalla-rectangles: cellular localization of compounds and their antiproliferative activities. *Chem. Commun.* **2016**, *52*, 4274−4277.
(50) Gupta, G.; Cherukommu, S.; Srinivas, G.; Lee, S. W.; Mun, S. H.; Jung, J.; Nagesh, N.; Lee, C. Y. BODIPY-based Ru(II) and Ir(III) organometallic complexes of avobenzone, a sunscreen material: Potent anticancer agents. *J. Inorg. Biochem.* **2018**, *189*, 17−29.
(51) Gupta, G.; Kumari, P.; Ryu, J. Y.; Lee, J.; Mobin, S. M.; Lee, C. Y. Mitochondrial localization of highly fluorescent and photostable BODIPY-based ruthenium(II), rhodium(III), and iridium(III) metal complexes. *Inorg. Chem.* **2019**, *58* (13), 8587−8595.
(52) Geri, S.; Krunclova, T.; Janouskova, O.; Panek, J.; Hruby, M.; Hernández-Valdés, D.; Probst, B.; Alberto, R. A.; Mamat, C.; Kubeil, M.; Stephan, H. Light-activated carbon monoxide prodrugs based on bipyridyl dicarbonyl ruthenium(II) complexes. *Chem. - Eur. J.* **2020**, *26*, 10992−11006.
(53) Aksakal, N. E.; Tanrıverdi Eçik, E. T.; Kazan, H. H.; Yenilmez Çiftçi, G. Y.; Yuksel, F. Novel ruthenium(II) and iridium(III) BODIPY dyes: insights into their application in photodynamic therapy *in vitro*. *Photobiol. Sci.* **2019**, *18*, 2012−2022.
(54) Manders, E. M. M.; Verbeek, F. J.; Aten, J. A. Measurement of co-localization of objects in dual-colour confocal images. *J. Microsc.* **1993**, *169* (3), 375−382.
(55) Zhang, R.; Qin, X.; Kong, F.; Chen, P.; Pan, G. Improving cellular uptake of therapeutic entities through interaction with components of cell membrane. *Drug Delivery* **2019**, *26* (1), 328−342.
(56) Mazuryk, O.; Magiera, K.; Rys, B.; Suzenet, F.; Kieda, C.; Brindell, M. Multifaceted interplay between lipohiplicity, protein interaction and luminesecence parameters of non-intercalative ruthenium(II) polypyridyl complexes controlling cellular imaging and cytotoxic properties. *JBIC, J. Biol. Inorg. Chem.* **2014**, *19*, 1305−1316.
(57) Perillo, B.; Di Donato, M.; Pezone, A.; et al. ROS in cancer therapy: the bright side of the moon. *Exp. Mol. Med.* **2020**, *52*, 192−203.
(58) Murphy, M. P. How mitochondria produce reactive oxygen species. *Biochem. J.* **2009**, *417*, 1−13.
(59) Golbaghi, G.; Groleau, M.-C.; López de los Santos, Y.; Doucet, N.; Déziel, D.; Castonguay, A. Cationic RuII cyclopentadienyl complexes with antifungal activity against several *Candida* species. *ChemBioChem* **2020**, *21* (21), 3112−3119.
(60) Oliveira, K. M.; Honorato, J.; Demidoff, F. C.; Schultz, M. S.; Netto, C. D.; Cominetti, M. R.; Correa, R. S.; Batista, A. A. Lapachol in the design of a new ruthenium (II)-diphosphine complex and a promising anticancer metallodrug. *J. Inorg. Biochem.* **2021**, *214*, 111289.
(61) Rodrigues, F. P.; Carneiro, Z. A.; Mascharak, P.; Curti, C.; da Silva, R. S. Incorporation of a ruthenium nitrosyl complex into liposomes, the nitric oxide released from these liposomes and HepG2 cell death mechanism. *Coord. Chem. Rev.* **2016**, *306*, 701−707.
(62) Bakewell, S.; Conde, S.; Fallah, Y.; McCoy, M.; Jin, L.; Shajahan-Haq, A. N. Inhibition of DNA repair pathways and induction of ROS are potential mechanisms of action of the small molecular inhibitor BOLD-100 in breast cancer. *Cancers* **2020**, *12* (9), 2647.
(63) Sureshbabu, V. V.; Lalithamba, H. S.; Narendra, N.; Hemantha, H. P. New and simple synthesis of acid azides, ureas and carbamates from carboxylic acids: application of peptide coupling agents EDC and HBTU. *Org. Biomol. Chem.* **2010**, *8*, 835−84.
(64) Bittner, S.; Assaf, Y.; Krief, P.; Pomerantz, M.; Ziemnicka, B. T.; Smith, C. G. Synthesis of *N*-acyl, *N*-sulfonyl, and *N*-phosphinylphospha-$\lambda^5$-azenes by a redox-condensation reaction using amides, triphenylphosphine, and diethyl azocarboxylate. *J. Org. Chem.* **1985**, *50*, 1712−1718.
(65) (a) Sheldrick, G. M. *SHELXTL, An integrated system for solving, refining, and displaying crystal structures from diffraction data*; University of Göttingen: Göttingen, Germany, 1981. (b) Sheldrick, G. M. *SHELXT* - Integrated space-group and crystal-structure determination. *Acta Crystallogr., Sect. A: Found. Adv.* **2015**, *A71*, 3−8.
(66) (a) Spek, A. L. *PLATON, A multipurpose crystallographic tool*; Utrecht University: Utrecht, The Netherlands, 2005. (b) Spek, A. L. *J. Appl. Crystallogr.* **2003**, *36*, 7−13.
(67) Magde, D.; Wong, R.; Seybold, P. G. Fluorescence quantum yields and their relation to lifetimes of rhodamine 6G and fluorescein in nine solvents: improved absolute standards for quantum yields. *Photochem. Photobiol.* **2002**, *75* (4), 327−334.
(68) El-Dossoki, F. I. Refractive index and density measurements for selected binary protic-protic, aprotic-aprotic, and aprotic-protic systems at temperatures from 298.15 to 308.15 K. *J. Chin. Chem. Soc.* **2007**, *54* (5), 1129−1137.
(69) Schindelin, J.; Arganda-Carreras, I.; Frise, E.; Kaynig, V.; Longair, M.; Pietzsch, T.; Preibisch, S.; Rueden, C.; Saalfeld, S.; Schmid, B.; Tinevez, J.-Y.; White, D. J.; Hartenstein, V.; Eliceiri, K.; Tomancak, P.; Cardona, A. Fiji: an open-source platform for biological-image analysis. *Nat. Methods* **2012**, *9* (7), 676−682.
(70) Bolte, S.; CordeliÈRes, F. P. A guided tour into subcellular colocalization analysis in light microscopy. *J. Microsc.* **2006**, *224* (3), 213−232.
(71) Costes, S. V.; Daelemans, D.; Cho, E. H.; Dobbin, Z.; Pavlakis, G.; Lockett, S. Automatic and quantitative measurement of protein-protein colocalization in live cells. *Biophys. J.* **2004**, *86* (6), 3993−4003.


https://doi.org/10.1021/acs.inorgchem.1c02929
*Inorg. Chem.* 2021, 60, 19152−19164